Volcano-tectonic interactions at Sabancaya volcano, Peru: eruptions, magmatic inflation, moderate earthquakes, and fault creep

Patricia MacQueen[1], Francisco Delgado[1,2], Kevin Reath[1], Matthew E Pritchard[1], Marco Bagnardi[3]*, Pietro Milillo[3], Paul Lundgren[3], Orlando Macedo[4], Victor Aguilar[4], Mayra Ortega[5], Rosa Anccasi[5], Ivonne Alejandra Lazarte Zerpa[5]†, Rafael Miranda[5]

[1]Cornell University, Ithaca, New York, USA
[2]Equipe de Tectonique et Mécanique de la Lithosphère, Institut de Physique du Globe de Paris, Université de Paris
[3]Jet Propulsion Laboratory, California Institute of Technology, Pasadena, California, USA
[4]Universidad Nacional de San Agustín de Arequipa, Arequipa, Perú
[5]INGEMMET Volcano Observatory (OVI)

Key Points:

- InSAR evidence for laterally and vertically complex volcanic plumbing system at Sabancaya
- High fluid pressure at Sabancaya promotes strong seismicity during 2012-2019 eruptive period
- High fluid pressure and static stress transfer from deep inflation promote long-lived fault creep

*Now at: NASA Goddard Space Flight Center, Greenbelt, Maryland, USA
†Now at: Instituto Geofísico del Perú, Lima, Perú

Corresponding author: Patricia MacQueen, pgm65@cornell.edu

Abstract

We present evidence of volcano-tectonic interactions at Sabancaya volcano that we relate to episodic magma injection and high regional fluid pore pressures. We present a surface deformation time series at Sabancaya including observations from ERS-1/2, Envisat, Sentinel-1, COSMO-SkyMed, and TerraSAR-X that spans June 1992 – February 2019. These data show deep seated inflation northwest of Sabancaya from 1992-1997 and 2013-2019, as well as creep and rupture on multiple faults. Afterslip on the Mojopampa fault following a 2013 M_W 5.9 earthquake is anomalously long-lived, continuing for at least six years. The best fit fault plane for the afterslip is right-lateral motion on an EW striking fault at 1 km depth. We also model surface deformation from two 2017 earthquakes (M_W 4.4 and M_W 5.2) on unnamed faults, for which the best fit models are NW striking normal faults at 1-2 km depth. Our best fit model for a magmatic inflation source (13 km depth, volume change of 0.04 to 0.05 km^3 yr^{-1}), induces positive Coulomb static stress changes on these modeled fault planes. Comparing these deformation results with evidence from satellite thermal and degassing data, field observations, and seismic records, we interpret strong pre-eruptive seismicity at Sabancaya as a consequence of magmatic intrusions destabilizing tectonic faults critically stressed by regionally high fluid pressures. High fluid pressure likely also promotes fault creep driven by static stress transfer from the inflation source. We speculate that strong seismicity near volcanoes will be most likely with high pore fluid pressures and significant, offset magmatic inflation.

1 Introduction

In several volcanic crises, tectonic activity on regional faults kilometers away from the volcanic edifice preceded renewed magmatic activity [*White and McCausland*, 2016]. *White and McCausland* [2016] summarize several such cases of precursory distal volcano-tectonic earthquakes ("distal VTs" or "dVTs") around the globe. These dVTs are often the earliest precursor to eruptive activity at volcanoes that have been dormant for decades or more. They begin weeks to years before the onset of volcanic activity, can occur kilometers from the volcanic edifice, and tend to die off sharply after the beginning of volcanic activity [*White and McCausland*, 2016]. *White and McCausland* [2016] propose a mechanism for dVTs in which intrusion of new magma into a volcanic system pressurizes surrounding aquifers, triggering earthquakes on pre-existing tectonic faults. They argue further that static stress changes from the intrusion [e.g., *King et al.*, 1994] are unlikely to be large enough to trigger slip on faults kilometers away.

Recent tectonic activity preceding and coincident with eruptive activity at Sabancaya volcano in southern Peru (Figure 1) displays many of the features attributed to distal VTs. The rich database of deformation, thermal [*Reath et al.*, 2019a,b], and seismic data available at Sabancaya provides an ideal data set for testing the *White and McCausland* [2016] interpretation and mechanism for distal VT events – a chance to test a proposed "common process at unique volcanoes" [*Cashman and Biggs*, 2014].

Sabancaya volcano is one of the most active volcanoes in the Central Andes [*Pritchard et al.*, 2018], with an ongoing period of unrest that began in 2012-2013 [*Jay et al.*, 2015]. Manifestations of unrest have included increased fumarolic activity, gas emissions, swarms of volcano-tectonic (VT) earthquakes, ground deformation, and explosions [*Reath et al.*, 2019a]. Explosions began in 2014, and reached a maximum of VEI 3 (volcanic explosivity index) in November 2016 [*Machacca Puma et al.*, 2018; *Global Volcanism Program*, 2017]. Eruptions at Sabancaya present a hazard to the surrounding region and Peru's second largest city, Arequipa (Figure 1), through ashfall and potential contamination of the drinking water supply [*Rankin*, 2012].

Several different faults surrounding the volcano have had shallow depth (< 30 km) moderate earthquakes ($M_W > 4.5$) during the recent unrest, over 20 within 50 km of Sabancaya since 2013. Few earthquakes were recorded teleseismically prior to early 2013

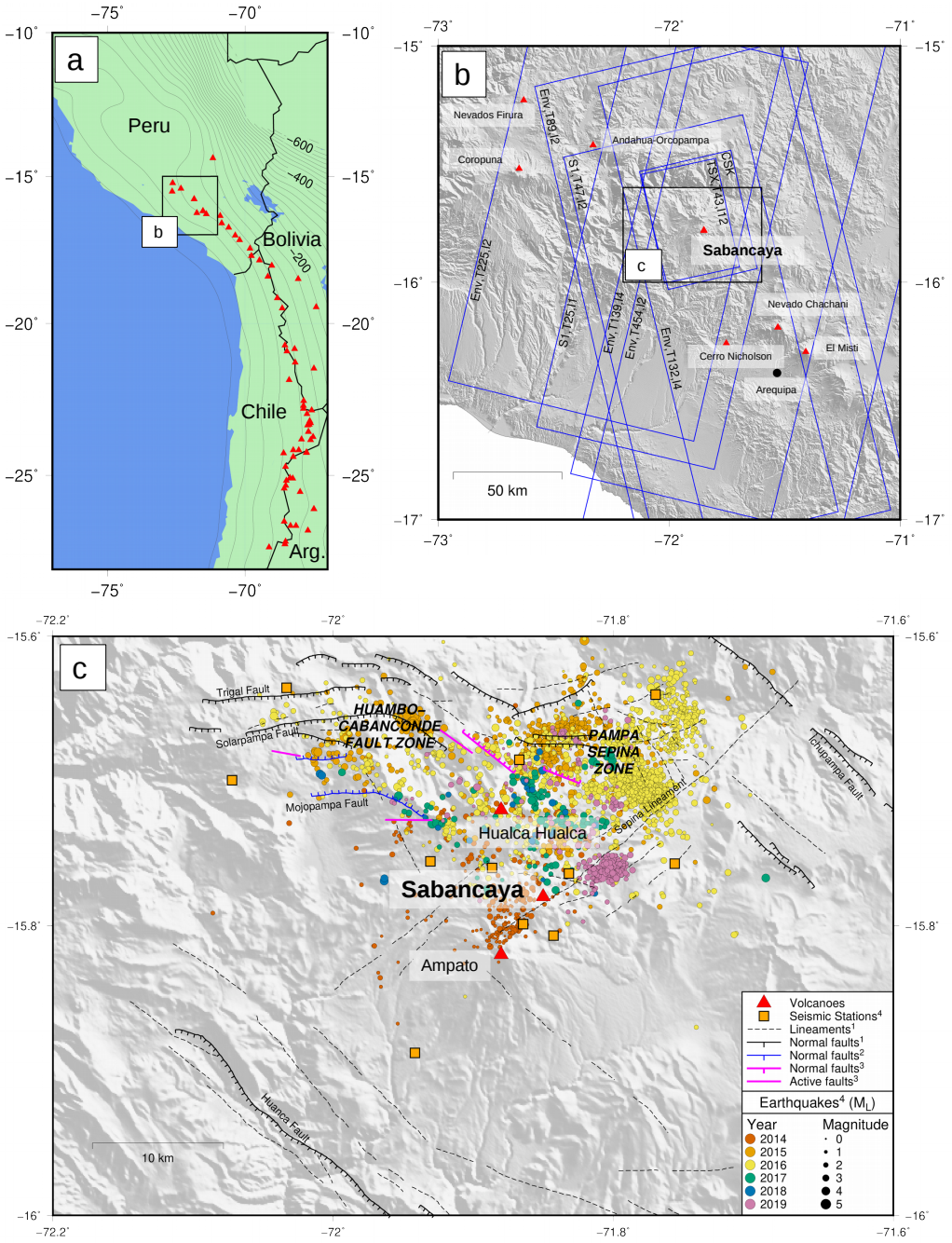

Figure 1. (a) Overview map of the Central Andean Volcanic Zone, with Holocene volcanoes [red triangles, *Global Volcanism Program*, 2013] and subduction slab contours [gray lines, *Hayes et al.*, 2012]. Black box denotes area shown in Figure 1b. (b) Map of southern Peru showing the location of Sabancaya. Blue rectangles indicate satellite tracks used in this study, and red triangles are Holocene volcanoes [*Global Volcanism Program*, 2013]. Black circle marks the location of Arequipa. Black box denotes area shown in Figure 1c. (c) Zoom-in map of the Sabancaya region. Red triangles mark locations of Sabancaya, Hualca Hualca, and Ampato. Faults and lineaments are from [1]*Antayhua et al.* [2002], [2]*Jay et al.* [2015], and [3]this study. Filled circles are earthquakes recorded by the [4]INGEMMET seismic network (orange triangles) from 2014 to 2019. Figure modified from Figure 1 in *Jay et al.* [2015].

near Sabancaya [*Jay et al.*, 2015]. The large number of earthquakes with $M_W > 4.5$ near a volcano without coincident eruption is globally unusual [*Zobin*, 2001; *Jay et al.*, 2015]. Given the close proximity in time and space of the elevated seismicity and eruptive activity at Sabancaya, a link between the two seems likely, but the nature of that link is unclear. A previous InSAR (Interferometric Synthetic Aperture Radar) study using very limited data from 2002 to 2015 found no evidence for magmatic deformation above the detection threshold [*Jay et al.*, 2015], although InSAR detected inflation had occurred between 1992 and 1997 during a previous eruptive episode [*Pritchard and Simons*, 2004]. Moreover, higher temporal resolution SAR data collected after 2015, covering the still ongoing eruption at Sabancaya, may help elucidate any connections between tectonic and magmatic activity.

An additional atypical feature of the tectonic activity near Sabancaya is the observation of potentially aseismic slip on multiple faults. *Jay et al.* [2015] observed possible creep across the Solarpampa fault, an aseismic component to an earthquake swarm in 2002, and afterslip on the Mojopampa fault [*Benavente et al.*, 2016] after it ruptured in a M_W 5.9 earthquake on 17 July 2013. These observations of fault creep are unique in a volcanic area in that they are not obviously related to flank gravitational motion, as is the case on other volcanoes [e.g., *Poland et al.*, 2017]. For crustal faults, fault creep is typically linked to changes in lithology along the fault, changes in the state of stress on the fault, and/or elevated pore pressure on the fault [e.g., *Bürgmann*, 2018; *Avouac*, 2015]. Determining what permits fault creep at Sabancaya would shed light on the state of stress in the shallow crust and what conditions favor aseismic versus seismic slip.

In this paper we investigate the following three research questions:

1. Is aseismic and seismic tectonic activity at Sabancaya related to magmatic activity, and if so, how?
2. By determining the driving tectonic forces at Sabancaya, can we identify the state of tectonic faults in the region?
3. What can ground and spaced based observations of unrest tell us about the dynamics of the magmatic system at Sabancaya?

To answer these questions we construct interferograms and InSAR times series at Sabancaya using data from several SAR satellites. We then use these deformation data to model deformation sources, and the static stress changes from these deformation sources, focusing on InSAR detected inflation, earthquakes, and aseismic slip. We finally combine these results with other information from seismic, thermal, and degassing data to form a conceptual model of magma-tectonic interactions at Sabancaya in which high pore fluid pressures facilitate aseismic slip and promote elevated seismicity in response to perturbations to the local stress field.

2 Overview of Sabancaya

Sabancaya is located in the Central Andean Volcanic Zone, one of the three volcanic zones in South America caused by the subduction of the oceanic Nazca plate beneath the South American continental plate (Figure 1a). The region around the volcano is cut by several active normal faults, striking primarily E-W and NW-SE, perpendicular to the overall direction of shortening in the arc [*Machare et al.*, 2003; *Mering et al.*, 1996; *Huaman-Rodrigo et al.*, 1993; *Sébrier et al.*, 1985](Figure 1c). *Dalmayrac and Molnar* [1981] theorize that this trench parallel normal faulting is due to the collapse of the highest elevation regions of the Andes, in which the compressive stresses causing thrust faulting in the lowlands are insufficient to support the highest elevation mountains.

Recent eruptive activity has included two eruptive episodes (max. VEI 3) from 1990 to 1998, and from 2012 to the time of this writing, with additional minor eruptive activity

(max. VEI 2) in the early 2000s [*Global Volcanism Program*, 2013]. Eruptive products range in composition from andesite to dacite [*Samaniego et al.*, 2016; *Gerbe and Thouret*, 2004], and long periods of repose (decades to centuries) are common [*Global Volcanism Program*, 2013; *Samaniego et al.*, 2016].

Increases in fumarolic activity heralded the reawakening of Sabancaya prior to its eruptions in the 1990s, after almost 200 years of dormancy [*Samaniego et al.*, 2016; *Gerbe and Thouret*, 2004; *Global Volcanism Program*, 2000; *Rodríguez and Uribe*, 1994; *Global Volcanism Program*, 1988; *Antayhua et al.*, 2001, 2002]. *Pritchard and Simons* [2004] later observed uplift produced by inflation of a deep seated source centered at Hualca Hualca (NE of Sabancaya) from 1992 to 1997. *Gerbe and Thouret* [2004] analyzed the products of the 1990-1998 eruptive sequence, and determined that a combination of magma mixing (andesite) and fractional crystallization (dacite), best explained the range from andesite to dacite in eruptive products.

Two phreatic explosions in August 2014 [*Jay et al.*, 2015; *Puma et al.*, 2016; *Global Volcanism Program*, 2016] ended a period of relative quiet from 1998 to 2014. Prior to the 2014 eruption, the area again experienced elevated levels of seismicity, culminating in a M_W 5.9 earthquake west of Hualca Hualca on the Mojopampa fault [Figure 1 on 17 July 2013, and Figure S1, *Puma et al.*, 2016; *Jay et al.*, 2015]. *Jay et al.* [2015] analyzed a limited SAR data set and seismic records for a series of earthquakes that preceded the 2014 eruption, but did not detect any magmatic deformation with the available data and analysis methods used (*Jay et al.* [2015] did not calculate any deformation time series). ASTER satellite measurements also detected volcanic thermal anomalies at Sabancaya. Beginning in 2011 these anomalies steadily increased first in temperature, and then in area [Figure S2, *Reath et al.*, 2019b]. During this time the plume consisted primarily of magmatic gasses with only trace amounts of ash [Figure S4, *Machacca Puma et al.*, 2018; *Global Volcanism Program*, 2016].

In November of 2016 eruptive activity increased dramatically in intensity, changing from a diffuse plume of mainly magmatic gasses to an ash-rich plume with several explosions per day [Figure S4, *Manrique Llerena et al.*, 2018; *Global Volcanism Program*, 2017]. *Kern et al.* [2017] measured extremely high emission rates of water vapor at Sabancaya in the six months prior to November 2016, consistent with the boiling off of the hydrothermal system. On 6 November 2016, vulcanian style explosions began [*Instituto Geofísico del Perú*, 2017]. After the onset of the November 2016 eruption, the thermal output at Sabancaya was high enough to saturate ASTER thermal measurements on the next two clear acquisitions (3 and 28 April 2017) [Figure S2, *Reath et al.*, 2019a]. In late 2016 a thermal anomaly at Hualca Hualca first became visible in ASTER satellite images, significantly increasing first in temperature and then area, similar to the thermal features on Sabancaya (Figure S2). Around this time, there were reports of an increase in the activity of pre-existing hydrothermal features in the area, and field observations found areas of hydrothermal activity co-located with the ASTER thermal anomalies [*Macedo*, 2018].

3 Data and Data Processing

In this study we use all available synthetic aperture radar (SAR) data from the Sentinel 1 A/B (S1), TerraSAR-X (TSX), and COSMO-SkyMed (CSK) SAR satellite missions spanning 2013 to 2019 as well as limited Envisat and ERS-1/2 data from 1992 to 2010 (Table S1).

3.1 ERS-1/2 and Envisat

Only a few interferograms are available from ERS-1/2 and Envisat C-band (5.6 cm wavelength) satellites, and most have long temporal and/or perpendicular baselines (Table S1). Thus, the time series for these datasets are noisier than for the more recent data.

Both datasets were processed using the ROI_PAC software package [*Rosen et al.*, 2004] – the Envisat data by *Jay* [2014] and ERS-1/2 by *Pritchard and Simons* [2004].

To calculate a time series with the ERS-1/2 data, we used the the deformation source calculated for each interferogram in *Pritchard and Simons* [2004] to forward model the predicted deformation at Sabancaya. We used the time-series approach of *Henderson and Pritchard* [2013] to calculate a time series using the Envisat data.

3.2 COSMO-SkyMed

We used SAR data from the Italian Space Agency (ASI) COSMO-SkyMed (CSK) X-band (3.1 cm wavelength) four-satellite constellation. Data are from the ascending pass of the satellite. CSK data were processed using the InSAR Scientific Computing Environment (ISCE) package developed at the Jet Propulsion Laboratory (JPL), Caltech, and Stanford University [*Rosen et al.*, 2015]. ISCE processing used the Shuttle Radar Topography Mission (SRTM) 30 m digital elevation model [*Farr et al.*, 2007] to correct for topography. For interferogram unwrapping we used the SNAPHU unwrapper [*Chen and Zebker*, 2001] implemented in ISCE.

Perpendicular baselines for the CSK data were generally constrained to be within 400 m and 3 months in orbital and temporal separation, respectively. For each acquisition, we then selected the four shortest (in time) pairs meeting the requirements mentioned above (e.g., 1-2, 1-3, 1-4, 1-5; 2-3, 2-4, 2-5, 2-6. . .).

We computed InSAR time series from such sets of 348 interconnected interferograms using the GIAnT software package [*Agram et al.*, 2012] in the NSBAS mode. Atmospheric corrections were not applied, as the smaller spatial footprint makes estimation of atmospheric effects harder, and the signals of interest were large enough that such corrections were not needed.

3.3 TerraSAR-X

We calculated interferograms for the TSX time series (originally calculated for *Reath et al.* [2019a]) with perpendicular baselines less than 100 m and temporal baselines less than 1 year using the ROI_PAC software package [*Rosen et al.*, 2004]. We then down-looked interferograms by 8 looks with a power spectrum filter strength between 0.2 and 0.5 [*Goldstein et al.*, 1988], unwrapped them with the SNAPHU algorithm [*Chen and Zebker*, 2001], and co-registered them using the "ampcor" routine in ROI_PAC [*Rosen et al.*, 2004].

We calculated the TSX time series with a MATLAB implementation of the SBAS time series method of *Berardino et al.* [2002], with no Digital Elevation Model (DEM) error correction, that has been used in many other publications [*Finnegan et al.*, 2008; *Henderson and Pritchard*, 2013, 2017; *Delgado et al.*, 2017]. DEM error corrections were not attempted because the pairs have a small temporal baseline and the satellite baseline does not drift during the acquisition time. In order to avoid removing signals of interest, no atmospheric corrections were applied, nor ramps removed, because of the small area of the TSX swath relative to the signals of interest. We instead referenced every interferogram to a stable area south of the deforming area. We found that this approach of removing a spatially constant offset did not change the results significantly with respect to removing ramps in the small non-deforming areas at Sabancaya.

3.4 Sentinel 1

We used the ISCE software package [*Rosen et al.*, 2015] to process interferograms for the S1 dataset, using the SRTM 30 m digital elevation model [*Farr et al.*, 2007] to correct for topography. We chose interferograms to process for the S1 time series via a

"daisy-chain" method in which for each SAR scene we created interferograms with the next three SAR scenes chronologically. We did not use a single master SLC to create a common simulation for the whole data set. This maintains small temporal baselines, while also ensuring that each time interval is covered by multiple interferograms in case one of the interferograms has burst alignment issues [potentially due to ionospheric perturbations, e.g., *Wang et al.*, 2017] or unresolvable unwrapping errors. We downlooked the S1 interferograms using 2 looks in azimuth and 8 looks in range. These interferograms were first unwrapped using the GRASS algorithm [*Goldstein et al.*, 1988], and if unwrapping errors were found we redid the unwrapping using the SNAPHU algorithm [*Chen and Zebker*, 2001]. After the second pass of unwrapping, interferograms that still had unwrapping errors or burst alignment errors [e.g., *Wang et al.*, 2017] were excluded from later time series calculations.

We calculated deformation time series from the S1 interferograms with the SBAS method [*Berardino et al.*, 2002] using the open source software package GiANT [*Agram et al.*, 2012]. As the spatial footprint of the S1 radar images is much larger than the signals of interest, we were able to use the methods of *Lin et al.* [2010] to apply an empirical correction for topography-related stratified atmosphere effects to the S1 time series. This correction reduced the temporal variance of pixels in areas of high relief, particularly near the canyon north of Hualca Hualca.

We processed selected S1 interferograms for earthquake modeling with less downlooking to create higher resolution interferograms, using 1 look in azimuth and 4 looks in range. These interferograms were unwrapped using the SNAPHU algorithm [*Chen and Zebker*, 2001]. We masked regions of low coherence and unwrapping errors prior to modeling.

4 Modeling Strategy

In this paper we infer deformation sources for InSAR-measured deformation from two 2017 earthquakes, inflation, and a creeping fault using analytical deformation source models. These analytical models are a vast simplification of complex geology, assuming a semi-infinite, elastic, isotropic, homogeneous half-space [*Mogi*, 1958; *Yang et al.*, 1988; *Newman et al.*, 2006]. However, they are still useful for getting a first-order picture of the different sources of deformation at Sabancaya that will allow us to investigate any interactions between these deformation sources over the time periods of months-years.

To solve for a deformation source for the deep-seated inflation, we first downsampled surface deformation [*Lohman and Simons*, 2005] rate maps calculated from the S1 time series (ascending and descending tracks) and the TSX time series (ascending track only), as the inflation rate is roughly linear over the time period of observation. We used the Neighborhood Algorithm [*Sambridge*, 1999] to find best fit parameters for a spherical source [*Mogi*, 1958], and a vertical prolate ellipsoid [*Newman et al.*, 2006; *Yang et al.*, 1988].

For calculating the earthquake deformation sources, we used S1 interferograms spanning the event as close in time as possible, with as high a coherence as possible. We did not remove a model of the inflation from these interferograms prior to performing modeling, as the inflation signal is below the level of the noise in these interferograms. We downsampled this data using the method described in *Lohman and Simons* [2005]. Using a Neighborhood Algorithm [*Sambridge*, 1999], we first found parameters for a uniform-slip fault plane embedded in a homogeneous elastic half-space [*Okada*, 1985] that best matched the data. Next, we used this best-fit fault plane to solve for distributed slip with triangular dislocations using the algorithms of *Barnhart and Lohman* [2010].

We modeled the time series for aseismic movement on the Mojopampa fault (Figure 1) using the analytical expression of *Perfettini and Avouac* [2004]:

$$\delta(t) = \delta_i + \frac{aH\sigma}{G} log \left[1 + d\frac{V_i}{V_0}(exp(t/t_r) - 1)\right] \quad (1)$$

Equation 1 calculates afterslip on a fault as a result of post-seismic rate-strengthening creep in response to a dynamic or static stress perturbation. In this expression, δ_i is the initial slip, a is a unitless rate dependent frictional parameter, H is the characteristic length of the rate-strengthening area, σ is the effective normal stress, and G is the shear modulus, and t_r is the characteristic time of the afterslip. V_i and V_0 are the initial creep velocity and interseismic plate velocity, respectively. d is a unitless parameter that characterizes the change in sliding velocity in response to a coseismic shear stress change.

We solved for δ_i, t_r, and the parameter combinations $\frac{aH\sigma}{G}$ and $d\frac{V_i}{V_0}$ using the Neighborhood Algorithm [*Sambridge*, 1999] to find the best fit to the measured line-of-sight displacement across the Mojopampa fault.

To model the deformation source for the creep on the Mojopampa fault, we first downsampled [*Lohman and Simons*, 2005] surface deformation maps calculated from the TSX time series spanning November 2013 to December 2016. We then found the best-fit parameters for a uniform-slip fault plane [*Okada*, 1985] using the Neighborhood Algorithm [*Sambridge*, 1999].

To calculate coulomb static stress changes from the volcanic inflation and earthquakes, we used the Coulomb3.4 Matlab package by S. Toda (`https://earthquake.usgs.gov/research/software/coulomb/`), that uses the methods developed in *King et al.* [1994]. We used the best fit spherical source model as the coulomb static stress source and receiver for magmatic inflation. InSAR modeled fault planes from this study and *Jay et al.* [2015] served as both sources and receivers in our calculations.

5 Results

Figures 2 and 3 show rates of InSAR detected deformation at Sabancaya from 2013-2019. A broad zone of uplift is evident in the CSK, TSX, and S1 time series (Figures 2 and 3), centered northwest of Sabancaya near Hualca Hualca. Figure 3 also shows deformation from seismic slip on two faults north of Hualca Hualca. Figure 2b and d feature aseismic slip on three faults west of Hualca Hualca, while Figure 3c and d shows creep continuing on the Mojopampa fault following the 17 July 2013 earthquake through 2019 [*Jay et al.*, 2015].

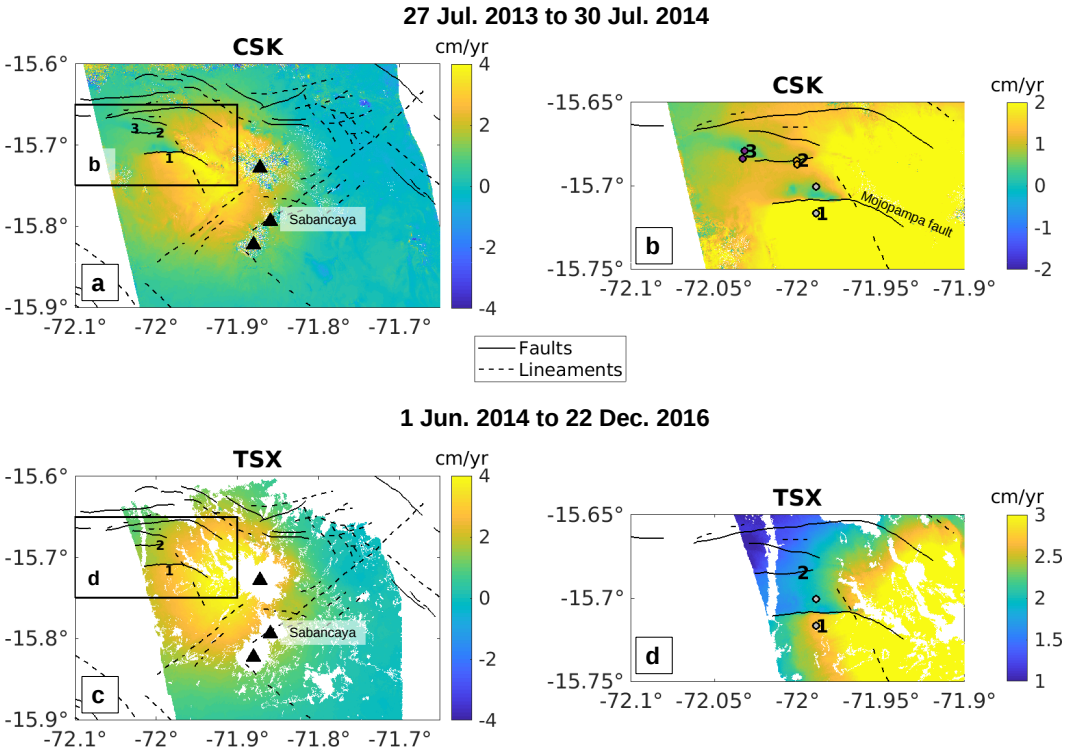

Figure 2. Maps of rate of ground displacement in satellite line-of-sight at Sabancaya showing deformation from fault creep and the beginnings of inflation at Hualca Hualca. (a) and (b) show displacement rates calculated from a linear time series from CSK data spanning 27 July 2013 to 30 July 2014. (c) and (d) show displacement rates calculated from a linear time series from TSX data spanning 1 June 2014 to 22 December 2016. Note that color scales are different between (a) and (b), and between (c) and (d) to better show fault creep in (c) and (d). Although the CSK and TSX time series both span the 17 July 2013 M_W 5.9 earthquake [modeled by *Jay et al.*, 2015], these figures do not span the earthquake. Numbers and colored dots indicate locations of time series points shown in Figure 8. Volcanoes are marked with black triangles. Faults and lineaments are from *Jay et al.* [2015] and *Antayhua et al.* [2002].

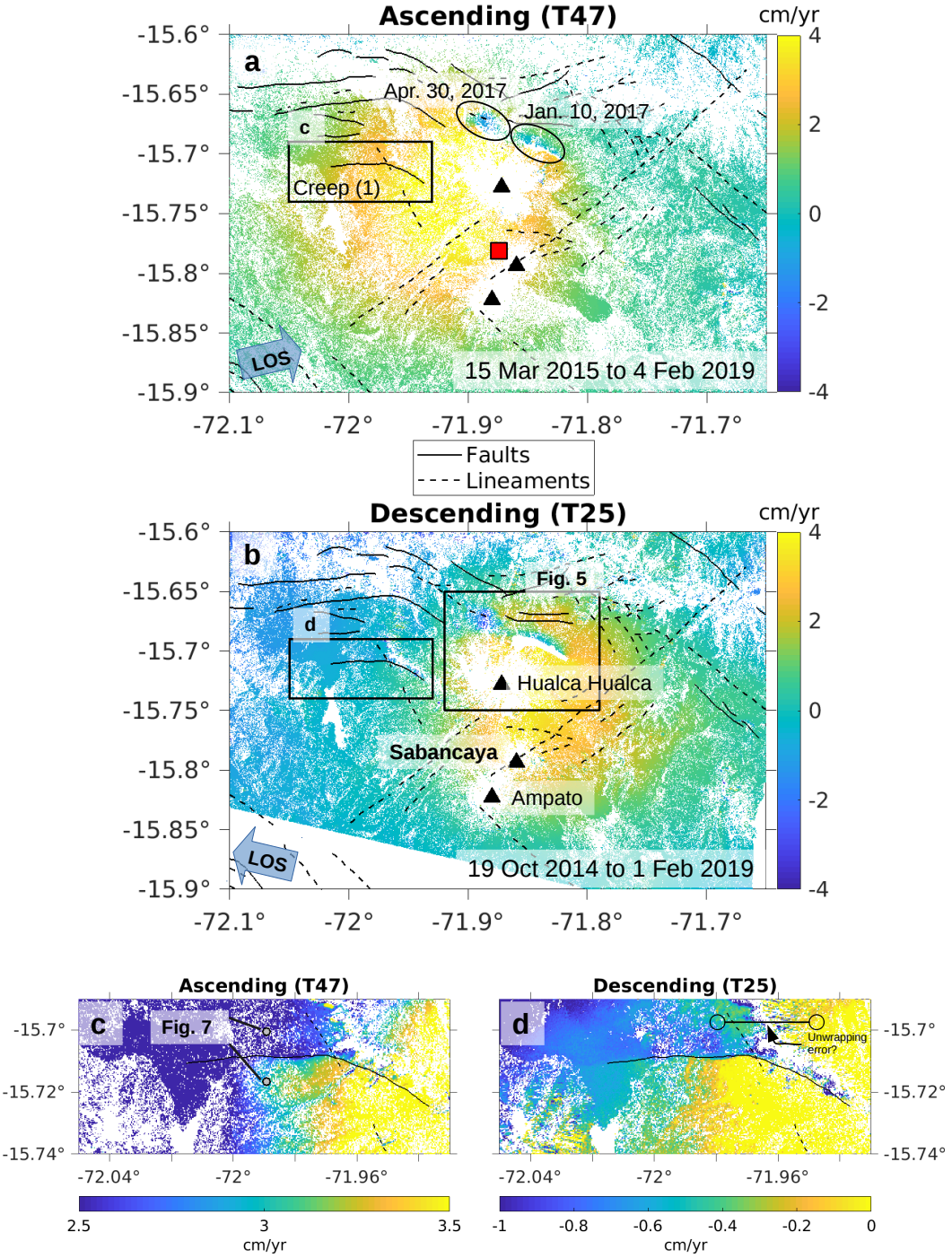

Figure 3. Maps of rate of line-of-sight deformation at Sabancaya showing deformation from inflation, fault creep (black rectangle in (a)), and two earthquake events (black ellipses in (a)) for the ascending (a) and descending (b) S1 tracks. Deformation rates are calculated from a linear time series from S1 data spanning 15 March 2015 to 4 February 2019 and 19 October 2014 to 1 February 2019 for the ascending and descending tracks, respectively. Volcanoes are marked with black triangles. Faults and lineaments are from *Jay et al.* [2015] and *Antayhua et al.* [2002]. Black rectangle in (a) indicates area depicted in (c) and (d), and red square is the location of the time series in Figure 10. Black rectangle in (b) indicates area depicted in Figure 5. (c) and (d) show a zoom-in on the Mojopampa fault/Creeping Fault 1 (Figure 2). Gray dots in (c) show the points subtracted in Figure 8 to show the evolution of aseismic slip with time. Note that color scales are different between (a) and (b), and between (c) and (d) to better show fault creep in (c) and (d).

5.1 Inflation source

The uplift rate between 2013 and 2019 creates a maximum line-of-sight displacement of approximately 3-4 cm yr^{-1} in the CSK, TSX, and S1 time series, with the point of maximum displacement located at Hualca Hualca (Figures 2 and 3). The spatial footprint of the deformation signal is similar to that in *Pritchard and Simons* [2004] during the 1992-1997 time period.

Using a spherical source [*Mogi*, 1958], the best fit model for the S1 time series (ascending and descending tracks) places the inflation at a depth of 13 km with a volume change of about 0.04 km^3 yr^{-1} (Figure 4), located within 3 km of the deformation source calculated for the 1992-1996 inflation [*Pritchard and Simons*, 2004]. The suite of acceptable models generated by the neighborhood algorithm [*Sambridge*, 1999], defined as having misfit within 5% of the best fit model, yields depths ranging from 12 to 15 km, and volume changes ranging from 0.03 to 0.05 km^3 yr^{-1}. We achieved similar results using a spherical source to model the TSX data (ascending track only), with a depth of 14 km and a volume change of 0.05 km^3 yr^{-1}. Using both the S1 and TSX time series, the center of the inflation is centered at the inactive volcano Hualca Hualca, approximately 7 km NNW of Sabancaya. Inversion results for the inflation source with and without models of the 2017 earthquakes removed are not significantly different, so we did not remove the earthquake signals in the final inversion. These results for the depth and location of the source are consistent with modeling results for a spherical source using GPS data from 2014-2015 that find a source depth of 13 km [*Taipe Maquerhua et al.*, 2016].

Modeling the uplift with a prolate ellipsoidal source does not significantly improve the model fit to data (Figure S5). The best fit prolate ellipsoidal source [*Newman et al.*, 2006; *Yang et al.*, 1988], using a shear modulus of 28 GPa, has a depth of 13 km, a semi-major axis of 8 km, a semi-minor axis of 6 km, and a pressure change of 1.2 MPa yr^{-1}. An F-test between the two inversions gives a 98% chance of no significant difference between the two modeling scenarios, so we continue our analysis using the spherical source. The best-fit ellipsoidal source also has an aspect ratio of 0.7, approaching that of a sphere, strengthening the argument for using the simpler spherical source.

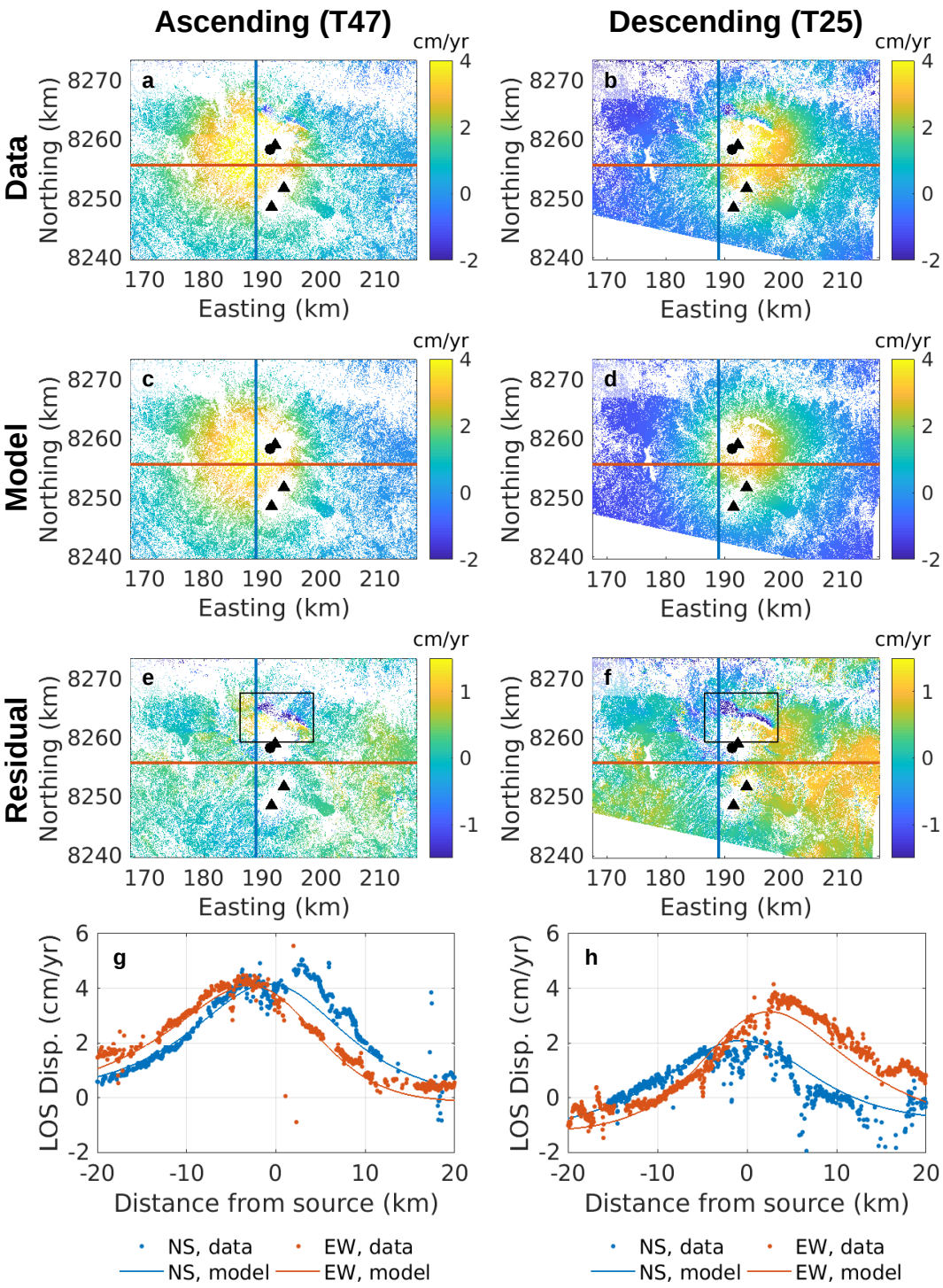

Figure 4. Spherical source modeling results for inflation source, using rate maps for ascending and descending S-1 a/b data spanning 2014-2019 (Figure 3). Top row is original data (full resolution), second row is forward modeled data, third row is the residual between the data and modeled data. The final row shows NS (orange) and EW profiles (blue) of data (dots) and forward modeled data (lines). Profiles are plotted as colored lines in the first three rows. The deformation signals from the 2017 earthquakes (black rectangles in (e) and (f)) were not removed prior to inversion, as tests showed that inversions removing the earthquake deformation model (Figure 5) produced no significant difference in the spherical source parameters.

5.2 2017 Earthquakes

Multiple S1 interferograms spanning January 10, 2017 show a northwest-southeast trending region of subsidence and uplift to the northeast of Hualca Hualca (Figure 5 A and B). The seismic catalog from the local seismic network records one M_L 4.4 earthquake on this date. To model this event we used two unwrapped interferograms from the ascending and descending tracks (Table S2).

InSAR modeling of this event gives M_W 5.0 for slip on a normal fault striking northwest dipping 89 degrees to the northeast, a slightly larger magnitude than that calculated from the local seismic network (Figure 6). The discrepancy in magnitude is small and may reflect the inherent uncertainty in both estimates of magnitude, but could indicate a small portion of the deformation occurred aseismically, potentially as afterslip that is seen after other earthquakes in the region. A distributed slip inversion shows that most of the slip occurs at 1.5 km depth, with a small region of higher magnitude slip at less than 0.5 km depth (Figure 7j). This concentration of high magnitudes of slip near the surface suggests that there may have been surface rupture associated with this event. However, evidence for this is ambiguous in the interferogram, as zones of low coherence along the fault are concentrated on a ridge, potentially indicating surface disruption (such as small landslides) rather than surface rupture. We discuss the difference in depth between the InSAR results and seismic catalogs in section 6.1.

The local seismic catalog records 5 events on 30 April 2017, all located to the north of Hualca Hualca, with the largest event having a local magnitude of 5.2. S1 interferograms spanning this date show an area of subsidence north of Hualca Hualca (Figure 5 c and d). To model this event we used an unwrapped interferogram from the ascending track (Table S2). We did not use any interferograms from the descending track to model this event as all descending interferograms covering this event suffered from unresolvable unwrapping errors.

Modeling of this interferogram gives a M_W 5.2 for oblique slip on a northwest striking normal fault dipping 54 degrees to the northeast, in good agreement with the local seismic network (Figure 6). A distributed slip inversion shows that most of the slip is concentrated at 1.5 km depth (Figure 7k).

The distributed slip inversion residuals show a low amplitude (4 cm) but spatially coherent area of negative residual (Figure 7). We interpret this as deformation from slip on another smaller magnitude event on the same day. The local seismic catalog shows a M_W 4.1 event nearby at less than 10 km, providing a likely candidate for this event. Attempts to model the residual with slip on a uniform fault plane [*Okada*, 1985] give mixed results. The best fit model is a normal fault with a strike of 250 degrees and a very shallow dip of 13 degrees. While the strike is broadly consistent with the observed deformation (Figure 5c) and regional fault strikes, the shallow dip is inconsistent with dip of faults in the area, typically between 60 and 70 degrees *Machare et al.* [2003]; *Mering et al.* [1996]; *Sébrier et al.* [1985]. Further, earthquakes on shallowly dipping normal faults are very rare and not predicted by most physical models [*Abers*, 2009]. It is likely that either the data was too contaminated by atmospheric noise to accurately constrain slip for the smaller event, or that a joint inversion of both fault planes simultaneously [e.g., *Frietsch et al.*, 2019] is necessary to constrain the geometry of both faults. It also also possible that the earthquake is best modeled by a curved and/or more complex fault geometry.

5.3 Creeping faults

Interferograms and time series from CSK, TSX, and S1 data reveal creep on three faults located northwest of Hualca Hualca (Figures 2 and 3). Creeping Faults 1 and 2 in Figure 2 are most likely the same faults that ruptured in the M_W 5.9 event on 17 July 2013 (Mojopampa fault), and the M_W 4.8 event on 25 July 2013, respectively, as observed

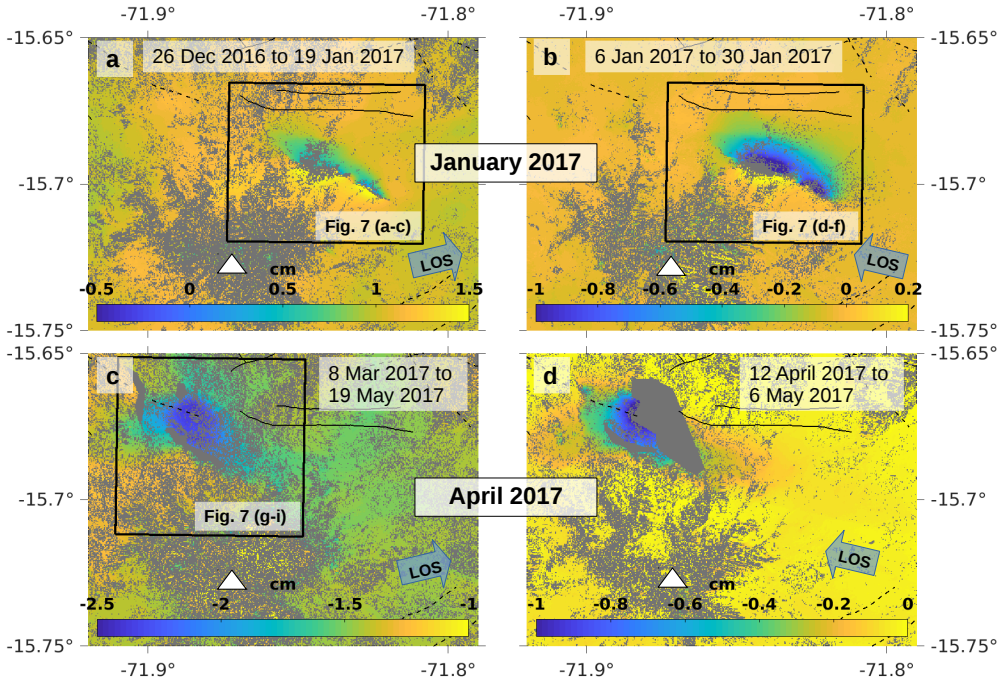

Figure 5. Unwrapped S1 interferogram spanning two small earthquakes – 10 January 2017 M_W 5.0 (top row) and 30 April 2017 M_W 5.2 (bottom row). A model of the inflation signal was not removed from this data (See section 4). Left column is data from the ascending track (T47) and the right column is from the descending track (T25). Hualca Hualca is marked with a white triangle. Faults and lineaments are from *Jay et al.* [2015] and *Antayhua et al.* [2002].

Date		InSAR	Local	NEIC	GCMT
10 January 2017	**Depth (km)**	1	12	3.9	-
	M_w	5.0	4.4	4.5	-
	Focal Mechanism	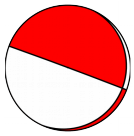	-	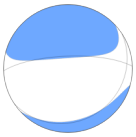	-
30 April 2017	**Depth (km)**	1.5	6.1, 8.7, 13, 13.6, 12.1	10, 10, 10	12, 21.7
	M_w	5.2	5.2, 4.1, 4.0, 4.0, 4.5	5.1, 4.6, 4.4	5.0, 4.9
	Focal Mechanism	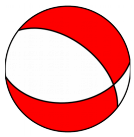	-	 -,-	 ,

Figure 6. Comparison of depths, magnitudes, and fault source parameters for earthquakes modeled in this study, calculated from InSAR, the IGP local seismic network, the Global CMT catalog, and the National Earthquake Information Center. Dashes (-) indicate no data.

by *Jay et al.* [2015]. Using a smaller SAR data set, *Jay et al.* [2015] also observed aseismic slip on Creeping Fault 1 (Mojopampa fault) during the first year after the 17 July 2013 earthquake.

Figure 8a shows line-of-sight displacement across Creeping Fault 1 from March 2013 to February 2019 using CSK, TSX, and S1 data, and Figure 8b shows line-of-sight displacement across Creeping Faults 2 and 3 from March 2013 to August 2014 using CSK data. In the first six months after the 17 July 2013 M_W 5.9 event, afterslip on Creeping Fault 1/Mojopampa fault was relatively rapid at a rate of 2-8 cm yr^{-1}. After about one year, the afterslip decayed to a constant rate of 0.5-0.6 cm/yr that continues to February 2019 (Figure 8a). Using Equation 1, we find a characteristic time t_r of 1.5 years best fits the data (black line in Figure 8a). For Creeping Faults 2 and 3, afterslip is much smaller magnitude (<2 cm in line-of-sight), and decayed to zero displacement after about five months.

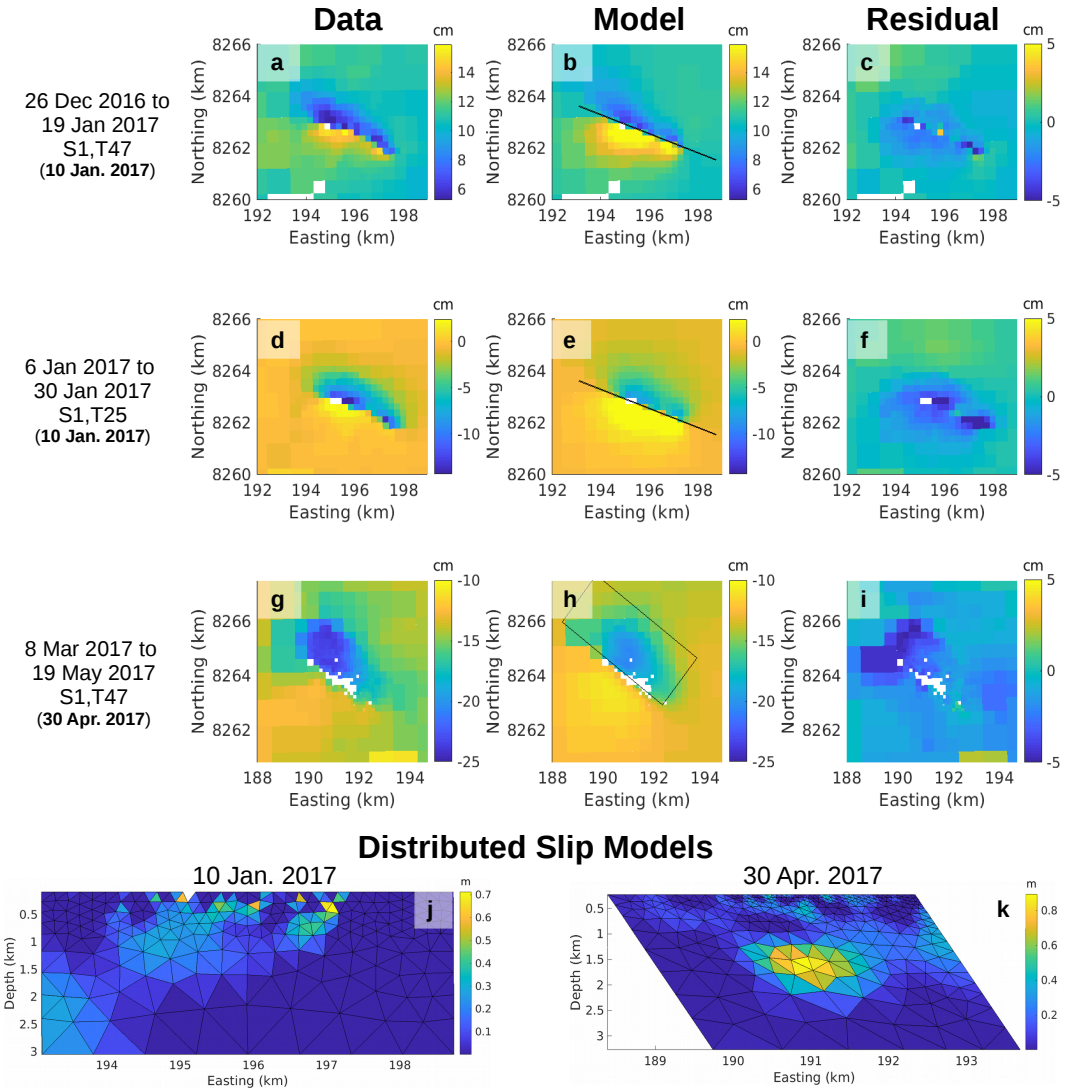

411 **Figure 7.** Modeling results for (from top to bottom) 10 January 2017 M_W 4.8 earthquake (T47 and T25)
412 and 30 April 2017 M_W 5.2 earthquake using S1 interferograms. A model of the inflation signal was not
413 removed from this data (See section 4). Left column is the downsampled data used in inversion, the cen-
414 ter column is forward modeled data from inferred distributed slip models with the XY coordinates of the
415 fault plane plotted (black rectangle), and the right column is the residual between data and forward modeled
416 data. (j) and (k) show the distributed slip models for the 10 January 2017 earthquake (j) and 30 April 2017
417 earthquake (k).

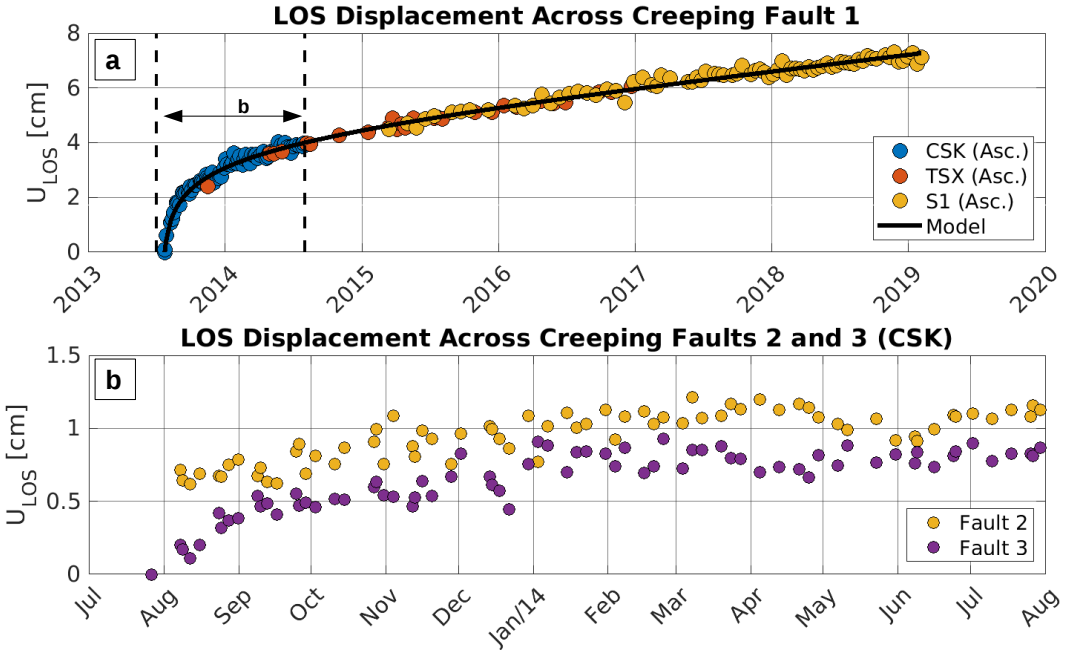

Figure 8. Line-of-sight displacements across creeping faults at Sabancaya. (a) Difference between points (black dots in Figure 3c) spanning Creeping Fault 1/Mojopampa fault (Figure 2) from 23 July 2013 to 4 February 2019 (gray dots in Figure 3c). Blue dots are from the CSK time series (23 July 2013 to 30 July 2014), and yellow dots are from the S1 time series (ascending, track 47, 15 March 2015 to 4 February 2019). Displacement is displayed relative to displacement in CSK time series on 23 July 2013. Black line is the best-fitting analytical function for frictional afterslip [*Perfettini and Avouac*, 2004]. (b) Displacement across Creeping Faults 2 and 3 (Figure 2) from 23 July 2013 to 30 July 2014, using CSK time series data.

The best-fit model for slip on Creeping Fault 1 (Mojopampa fault) is right-lateral motion at a depth of 1 km of an east-west striking fault dipping 78 degrees to the north, with a yearly moment release of M_w 4.4 (Figure S8). The location of the modeled slip is consistent with slip on the Mojopampa fault, at a shallower depth than the slip of the 2013 earthquake modeled in *Jay et al.* [2015]. The small amplitude of the surface deformation precluded distributed slip modeling. We did not attempt to model any aseismic slip on the eastern branch of the Mojopampa fault, as our InSAR data does not have resolution in that area of steep relief.

5.4 Seismic and aseismic active faults at Sabancaya, 1992-2019

Figure 9 shows a map of faults near Sabancaya with InSAR detected slip between 1992 and 2019 [this study, *Pritchard and Simons*, 2004; *Jay et al.*, 2015], along with ASTER satellite detected thermal anomalies [this study, *Reath et al.*, 2019a] and hydrothermal features mapped in the field [*Macedo*, 2018]. Faults where the sense of slip is shown via black hash marks have either been previously mapped in the field or modeled from InSAR data [this study, *Jay et al.*, 2015]. See Figures S6 and S7 in the supporting information for ERS and TSX interferograms that show fault slip in 1998 and 2013.

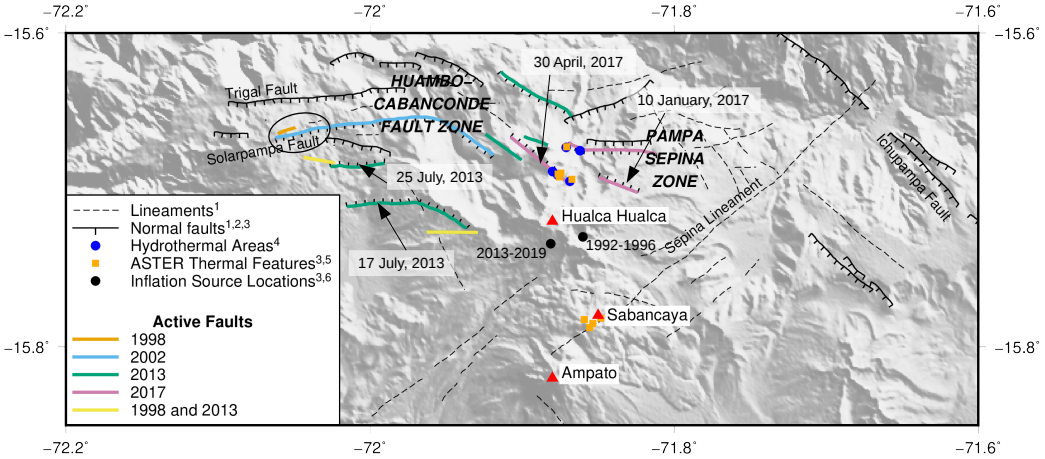

Figure 9. Active faults (seismogenic and aseismic) at Sabancaya imaged by InSAR (1998 to 2019), hydrothermal areas active from 2013 to 2019, and inflation sources active from 1992-1996 and 2013-2019 (See Figure 10). See Figures S6 and S7 in the supporting information for interferograms that show the active faults in 1998 and 2013. Faults related to a main earthquake event are labeled with the date of the earthquake. All other faults mapped as active represent likely secondary, triggered slip from a main earthquake event. Black ellipse marks section of the Solarpampa fault that slipped in 2002 [see Figure 2 of *Jay et al.*, 2015]. Faults and lineaments are from [1]*Antayhua et al.* [2002],[2]*Jay et al.* [2015], and [3]this study. Hydrothermal areas are from [4]*Macedo* [2018]. ASTER thermal anomalies are from [3]this study and [5]*Reath et al.* [2019a]. Inflation sources are from [3]this study and [6]*Pritchard and Simons* [2004].

InSAR detected slip is most frequently observed on the west, northwest, and north sides of Hualca Hualca (Figure 9). Interferograms that span large earthquakes in 1998 and 2013 show slip on multiple faults to the west of Hualca Hualca in both 1998 and 2013 (Figures S6 and S7). The hydrothermal activity at Hualca Hualca occurred directly on faults that ruptured in 2017 (Figure 9).

5.5 Coulomb static stress changes

The inflation source described above creates a positive Coulomb stress change (CSC) on the faults for the two 2017 earthquakes, as well as on Creeping Fault 1/Mojopampa fault (Figure S9). Assuming a start time for the inflation of May 2013 and a constant inflation rate, the January 2017 fault experienced an approximately 0.18 MPa increase in coulomb stress prior to slipping, and the April 2017 fault experienced an approximately 0.08 MPa increase. Although low, the increase in Coulomb static stress should be sufficient to promote slip on the January 2017 earthquake fault [*Wauthier et al.*, 2016; *Toda and Stein*, 2003]. However, the stress change on the April 2017 earthquake, although positive, is much less, so the evidence for static stress triggering on this fault is uncertain. Creeping Fault 1 also experienced a static stress increase of approximately 0.03 MPa/year, a cumulative static stress change of almost 0.2 MPa from May 2013 to February 2019. As for the 2017 earthquake faults, this magnitude of CSC should be enough to promote slip on this fault [*Wauthier et al.*, 2016; *Toda and Stein*, 2003].

We also found that the M_W 5.9 earthquake on the Mojopampa fault in 2013 did not cause a static stress change sufficient to promote slip on any of the 2017 earthquake faults. None of the earthquakes in 2017 caused a static stress change sufficient to promote slip on the Mojopampa fault. *Jay et al.* [2015] similarly found that static stress changes from seis-

mogenic faults in 2013 were insufficient to trigger any of the InSAR modeled earthquakes activity in 2013.

5.6 Timeline of activity at Sabancaya

Figure 10a summarizes activity at Sabancaya in the two previous eruptive episodes, compiling information from the *Global Volcanism Program* [2013]; *Reath et al.* [2019a,b], and this study. Strong seismicity, inflation, and significant hydrothermal activity characterized both the 1990s and current eruptive episode.

Figure 10c shows a time series of inflation and hydrothermal activity at Sabancaya from 1992 to 2019. The location of the inflation time series is marked as a red square in Figure 10b. The inflation time series includes data from ERS 1 and 2, ENVISAT, ALOS, TSX, and S1. The hydrothermal time series includes ASTER data at Sabancaya [previously published in *Reath et al.*, 2019a] and Hualca Hualca, and OMI degassing data [previously published in *Carn et al.*, 2017; *Reath et al.*, 2019a]. The inflation rate in the 2013-2019 eruptive episode is significantly higher than in the previous inflation from 1992 to 1996 [*Pritchard and Simons*, 2004]. For the current eruptive episode, inflation is first evident as of May 2013 in both the CSK and TSX time series (Figure 10). The roughly linear, increasing trend of uplift from 2013 to 2019 agrees with GPS observations beginning in 2016 that also show a similar, steady uplift [*Cruz et al.*, 2018; *Machacca Puma et al.*, 2018].

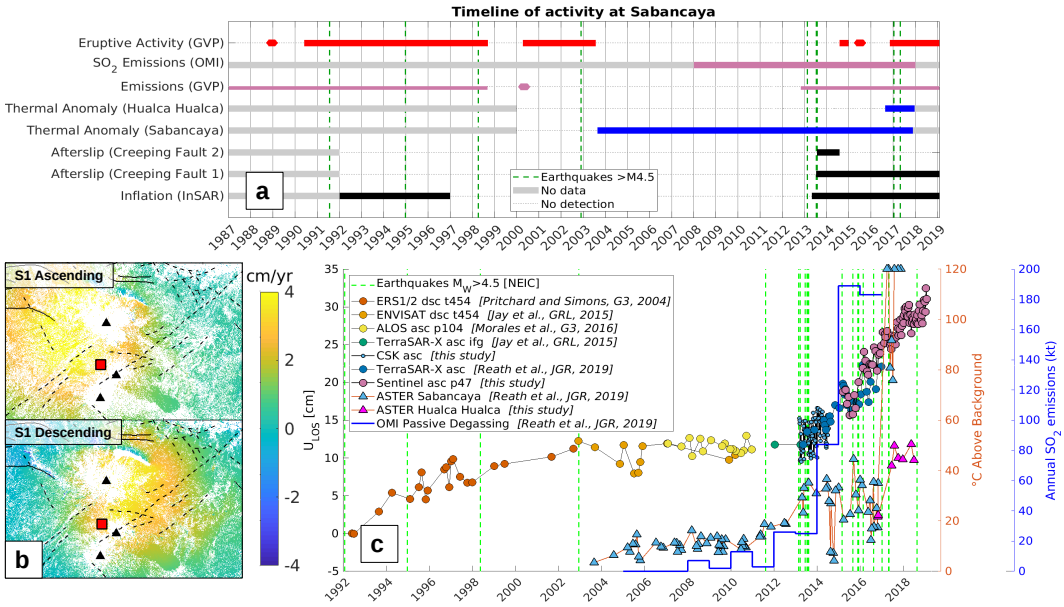

Figure 10. Timeline of activity at Sabancaya. Earthquakes > M_W 4.5 included in this figure are those studied by InSAR. See Figure S1 for times of all earthquakes > M_W 4.5 within 50 km of Sabancaya. (a) Summary of activity at Sabancaya with data from the *Global Volcanism Program* [2013], *Reath et al.* [2019a], *Pritchard and Simons* [2004], and this study. (b) For reference, S1 maps of rate of ground displacement from Figure 3 with location of time series in (c) marked with red square. (c) Inflation at Sabancaya and thermal anomalies at Sabancaya and Hualca Hualca. Line-of-sight inflation time series at Sabancaya (red square in (b) and Figure 3a) derived from ERS [*Pritchard and Simons*, 2004; *Jay*, 2014], ENVISAT [*Jay*, 2014; *Jay et al.*, 2015], ALOS [*Morales Rivera et al.*, 2016], TSX [*Reath et al.*, 2019a], and S1 (this study) data. Note that although this time series mixes ascending and descending data, the point at Sabancaya is chosen such that the amplitude of the uplift signal is as close as possible between ascending and descending. For the ALOS portion of the time series, we used the dates of the ALOS-1 images from *Morales Rivera et al.* [2016] and added synthetic noise with the same amplitude as the ERS and ENVISAT time series to simulate a time series with no deformation. Thermal data at Sabancaya originally published in *Reath et al.* [2019a].

6 Discussion

6.1 Discrepancies between InSAR and seismic catalog fault depths

The InSAR depths for the earthquakes modeled in this study are significantly shallower than the depths in the global catalogs (GMT, NEIC), although these discrepancies are consistent with those reported in other comparison of InSAR focal mechanisms and CMT catalogs, particularly given the small size (<M_w 6) of the events [e.g., *Devlin et al.*, 2012; *Holtkamp et al.*, 2011; *Weston et al.*, 2011]. The larger depth discrepancy for the January 2017 event between InSAR results and the local seismic catalog could be partially due to the velocity model used for the local catalog or the network geometry [*Mellors et al.*, 2004]. A full waveform inversion of local or teleseismic seismic records as in *Devlin et al.* [2012] could potentially reduce the discrepancy between InSAR and local and global seismic catalog depths, but this is beyond the scope of this study. *Mellors et al.* [2004] and *Gaherty et al.* [2019] find no significant difference between a homogeneous and heterogeneous half space model in their modeling of larger seismic events. We do not believe that the discrepancy can be explained as an effect of using homogeneous half-space modeling, rather than a more complex model. Visual inspection of the interferogram for the January and April 2017 earthquakes (Figure 5) also suggests that the earthquakes

are indeed much shallower than the depths listed in seismic catalogs. The interferograms are incoherent along the trace of the fault (incoherence masked in Figure 5), suggesting possible surface rupture. Based on this consideration of the possible causes of discrepancies between our results and other data sources, we conclude that the InSAR depths are more accurate than those from the local or global seismic catalogs.

6.2 Offset inflation at Hualca Hualca

The offset inflation observed at Sabancaya in both the 2010s and the 1990s [*Pritchard and Simons*, 2004], centered approximately 7 km NNW of Sabancaya, is not unique among volcanic systems. In a survey of volcanic deformation detected via satellite observations, *Ebmeier et al.* [2018] observes that 24% of detected deformation is centered more than 5 km from the nearest active volcanic edifice, which the authors interpret as compelling evidence for laterally extensive, complex magmatic plumbing systems [e.g., *Cashman et al.*, 2017]. The best fit spherical sources for both episodes of inflation at Sabancaya are within less than 5 km of each other, suggesting pressurization of the same zone of magma storage in both episodes. This offset inflation may illuminate activity in the deeper section of a laterally and vertically extensive complex of dikes and sills beneath Hualca Hualca, Sabancaya, and Ampato.

In both recent episodes of eruptive activity, the temporal behavior of the inflation does not correlate strongly with changes in eruptive behavior at the surface [Figure 10c, *Pritchard and Simons*, 2004; *Global Volcanism Program*, 2000]. Throughout the current eruptive sequence at Sabancaya, uplift continues linearly, without any changes in rate, even with the drastic change in eruptive activity in November 2016 (Figure 10c). However, the consistent observation of inflation in both of these eruptive episodes suggests some connection between the magma plumbing systems beneath Hualca Hualca and Sabancaya.

A possible interpretation of the offset inflation could be mafic recharge at depth, as proposed by *Gerbe and Thouret* [2004] for Sabancaya based on petrologic data, and suggested at other volcanic systems by measurement of excess SO_2 [e.g., *Edmonds et al.*, 2010, 2001]. In the model proposed by *Gerbe and Thouret* [2004], mafic recharge at depth induces magma mixing in a pre-existing dacitic magma reservoir slowly differentiating through open system crystallization. From our calculations in section 5.1, we suggest that the persistent inflation source at 13 km depth is the geophysical signature of this mafic recharge at depth. We speculate that mafic magma then moves laterally from a temporary zone of accumulation beneath Hualca Hualca to a shallower (6km), storage zone where magma mixing occurs between the fresh mafic magma and degassed, dacitic magma [e.g., *Gerbe and Thouret*, 2004], ultimately triggering eruptive activity at the surface. Temporary deflections in GPS-measured uplift at Sabancaya's summit immediately preceding increases in the number of hybrid earthquakes may be evidence for a smaller, shallow magma chamber near Sabancaya's summit [*Cruz et al.*, 2018]. Additionally, earthquake locations from 2015 to 2017 provide some evidence for possible magma transfer between Hualca Hualca and Sabancaya [*Anccasi Figueroa et al.*, 2018].

Voluminous degassing at Sabancaya suggests that the shallow magma storage zone is more open [*Kern et al.*, 2017; *Moussallam et al.*, 2017; *Reath et al.*, 2019a] (using the definition for "open" proposed by *Chaussard et al.* [2013]), perhaps explaining why no inflation has been observed centered at Sabancaya. This could explain the partial temporal disconnect between inflation episodes and eruptive activity, and fits with *Reath et al.* [2019a]'s classification of Sabancaya as "partially open". While the mafic intrusion reactivates the system and potentially induces magma mixing, triggering the whole sequence of unrest, it does not directly trigger pulses of eruptive activity.

6.3 Fault creep at Sabancaya

Aseismic movement on tectonic faults appears to be relatively common near Sabancaya, manifesting as fault creep, after-slip, and triggered slip. The InSAR time series in this study reveal aseismic fault movement on several faults northwest of Hualca Hualca (Figures 2,3, and 8). *Jay et al.* [2015] report possible aseismic movement in this area in the early 2000s based on the discrepancy between the cumulative seismic moment reported in earthquake catalogs and the seismic moment calculated from InSAR observed deformation. The authors also record creep on the Solarpampa fault in the same time period, although the magnitude of this creep is likely small.

Static stress transfer may be important for driving the long-lived aseismic slip on the Mojopampa fault (Creeping Fault 1 in Figures 8 and S9). After an initial period of afterslip, creep on this fault continues linearly, in tandem with the continuing inflation (Figures 8 and 10). Although long-lived afterslip on a normal fault is not unprecedented in this tectonic setting, the longest recorded afterslip in this region lasted for only one year [*Xu et al.*, 2019], far less than the 5+ years of creep observed in this study. For the Hayward fault in California, *Schmidt and Bürgmann* [2008] found that, after an earthquake, creep resumed when the ratio of shear to normal stress matched the value of this ratio prior to the earthquake. We posit that an optimal stress state caused by the inflation source may help drive the long-lived creep on the Mojopampa fault. Similarly, *Lundgren et al.* [2017] found that inflation at Copahue volcano also promoted aseismic normal slip on faults at the volcano's summit.

High pore fluid pressures likely also promote creep. The injection of fluids has been observed to induce aseismic slip on faults [*Bürgmann*, 2018], and rate-state friction modeling suggests that high pore fluid pressures should favor stable slip and extended afterslip [*Segall and Rice*, 1995]. Although all instances of fault creep occur in an area west of Sabancaya that lacks surface evidence of hydrothermal activity, the close timing between aseismic slip on the faults west of Hualca Hualca, and reinvigorated hydrothermal activity at Sabancaya (Figure 10), is suggestive of a link.

While static stress transfer from continuing inflation, along with high pore fluid pressures, may explain the long lived creep on the Mojopampa fault, this does not explain why this fault and others creep rather than rupture seismically. At other volcanoes, fault creep is often related to collapse of the volcanic edifice [e.g., *Poland et al.*, 2017]. However, we argue that the geometry of the creeping faults near Hualca Hualca are inconsistent with flank collapse, and are too far away from the summit of Hualca Hualca to be considered part of the flanks of the volcano.

Instead, lithological differences may explain the tendency for aseismic creep in this area. Geologic maps of the area near the creeping faults show outcrops of Jurassic age sedimentary rocks, in contrast to andesitic flows in the area near the 2017 earthquakes [*Benavente Escobar et al.*, 2018]. We propose that these sedimentary rocks exhibit rate-strengthening behavior that promotes aseismic slip. This is consistent with observations of extended afterslip in thicker sedimentary basins [e.g., *Lienkaemper and McFarland*, 2017]. More generally, multiple studies have identified lithological controls on the mode of fault slip along the length of a fault [e.g., *Bürgmann*, 2018; *Avouac*, 2015].

6.4 Connection between magmatic and tectonic activity

To establish any connection between seismicity and magmatic activity at Sabancaya, we must first rule out that the timing and location of the seismicity is simply due to local tectonics alone. The earthquakes modeled in this study and that of *Jay et al.* [2015] are consistent with regional fault trends, and the normal faulting observed in this study is expected in this region due to a rotation of the stress tensor in areas of high relief [*Dalmayrac and Molnar*, 1981; *Wimpenny et al.*, 2018; *Mering et al.*, 1996; *Devlin et al.*, 2012].

However, the region within 50 km of Sabancaya experienced no seismic activity between 2013 and the end of eruptive activity in 2002, except for one earthquake in 2011 (Figure S1). One possible explanation for the temporal clustering of seismicity in this region could be simple clustering of seismicity [e.g., *Marco et al.*, 1996; *Kagan and Jackson*, 1991]. However, shallow seismicity over the period of time covered by the NEIC catalog (1950 to 2019) is also spatially clustered around Sabancaya (Figure S10). We therefore consider the idea that the these tectonic earthquakes can be linked to the inflation observed at Sabancaya. We first investigate the mechanism of static stress transfer, and then consider the mechanism of a "fluid pressure pulse" [as in *White and McCausland*, 2016] by comparing the location and timing of hydrothermal activity and fault slip.

Static stress transfer from the inflation source should promote slip on regional faults, although static stress transfer alone is only likely to be sufficient after inflation has continued for a few years. Coulomb static stress change is positive for the faults analyzed in this study (Figure S9), which are representative of many of the faults that ruptured in this area [*Jay et al.*, 2015]. Analog models of caldera formation commonly predict normal faulting above an inflating source [*Acocella*, 2007]. By 2017, the buildup of static stress from ongoing inflation is sufficient to explain at least one of the two M_W 4.5+ earthquakes in that year.

However, the seismic activity in 2013 roughly coincides with the beginning of detectable inflation (Figure 10), when accumulated static stress from the inflation would be insufficient to promote slip. An alternative way to explain the earthquake activity in 2013 may be a fluid pressure pulse caused by an incipient volcanic intrusion [e.g., *White and McCausland*, 2016]. We have evidence of the reactivation of the hydrothermal system prior to the eruption from a satellite observed thermal anomaly at Sabancaya that increased in temperature and size around the time of the first phreatic eruption in 2013 [*Reath et al.*, 2019b], possible evidence of increased heat flow from a magmatic intrusion. *Kern et al.* [2017] measured anomalously high levels of water vapor in the plume from Sabancaya in 2016, evidence for aqueous fluids in the system prior to 2016. It may be that an increase in fluid pressure in the surrounding aquifers caused regional tectonic faults to slip early in their seismic cycle, as in the mechanism for "distal VTs" proposed by *White and McCausland* [2016].

Repeated triggered slip of regional tectonic faults suggests that the area around Sabancaya is at a critical state of stability. Figure 9 shows multiple smaller faults that slipped in both 1998 and 2013. The M_W 5+ earthquakes in both 1998 and 2013 appear to have triggered slip on several smaller surrounding faults, consistent with dynamic triggering from the larger earthquakes (Figures 9, S6, and S7). We interpret this as evidence that the area around Sabancaya is critically stressed by high fluid pore pressures, such that any stress perturbation in the area, whether from a large earthquake or a magmatic intrusion, will lead to a flurry of triggered slip on regional tectonic faults.

Aqueous fluids may have also influenced the 2017 earthquakes as well. Both satellite (Figure 10) and field observations [*Macedo*, 2018] show an increase in the area and intensity of a thermal anomaly on the north flank of Hualca Hualca (Figures 9, 10, and S2) beginning in 2016. These thermal anomalies are co-located with field observations of fumarole fields (Figure 9) that locals reported had increased the intensity of their emissions in 2018 [*Macedo*, 2018]. The trace of the April 2017 earthquake, when projected to the surface, aligns well with two of these fumarole fields [Figure 9, *Macedo*, 2018]. Both of the 2017 earthquakes occur in this region of reinvigorated hydrothermal activity. This suggests that increased pore pressure in the faults may have triggered slip on these faults in 2017, already primed to slip by static stress transfer from the inflation at depth.

While the evidence considered in this paper supports contributions from both static stress transfer and elevated fluid pore pressures to explain the strong seismicity at Sabancaya, our ability to determine the relative contributions of each of these mechanisms is

limited. Geophysical mapping of the extent of the subsurface hydrothermal system, for example using electrical methods [e.g., *Comeau et al.*, 2016; *Byrdina et al.*, 2013], could more accurately identify areas where we would expect high pore fluid pressures. Subsurface mapping of the hydrothermal system could also shed light on what determines the location of creep at Sabancaya. Further work could also include more detailed modeling of the fluid pressure pulse itself [e.g., *Miller et al.*, 2004], in order to better constrain the timing and magnitude of the pressure perturbation needed to trigger the observed seismicity.

6.5 Comparison with other volcanic systems

Multiple other volcanic systems have similar features to Sabancaya (deformation and/or extensive hydrothermal systems), but lack large earthquakes. We argue that the key factors contributing to large (>M_W 4.5) earthquakes at Sabancaya are the combination of (1) the magnitude of the deformation, (2) the extensive hydrothermal activity, and (3) uplift offset 5 km from the active volcano beneath an area of low heat flow that allows larger seismogenic faults. Ubinas volcano is located in southern Peru with a similar tectonic environment [*Dalmayrac and Molnar*, 1981] and volume of degassing [*Moussallam et al.*, 2017], but unlike Sabancaya does not experience significant deformation or large magnitude seismicity [Figure S10, *Global Volcanism Program*, 2013; *Reath et al.*, 2019a]. Similar to Sabancaya, Three Sisters Volcano in the United States experienced uplift in an area offset from the summit, in an area with likely low heat flow conducive to larger faults, but the area lacks any signs of hydrothermal activity [*Riddick and Schmidt*, 2011] that might point to high pore fluid pressures. Cordon Caulle [*Delgado et al.*, 2018] and Laguna del Maule [*Singer et al.*, 2018] in Chile, and Sierra Negra in the Galapagos, Ecuador [*Chadwick et al.*, 2006], have all experienced meter scale deformation. Of those three, only Sierra Negra has experienced large earthquakes in its trapdoor-faulting episodes [*Chadwick et al.*, 2006], which involve very large faults bounding the caldera.

Iwatesan volcano in Japan has many of the features we identify as crucial at Sabancaya for promoting large earthquakes, and in 1998 a M_W 6.1 earthquake occurred on a known Quaternary fault close to the volcano [*Nishimura et al.*, 2001]. The volcano has a well-known geothermal area, and beginning months before the earthquake, InSAR satellite measurements detected uplift offset from the edifice [*Nishimura et al.*, 2001]. *Nishimura et al.* [2001] calculated a volume change of 0.03 km^3, comparable to what we find for Sabancaya, and found that the Coulomb static stress change from the inflation promoted slip on the fault that ruptured. This example shows a positive example of how magmatic inflation, an extensive hydrothermal system but limited heat flow above the deformation source, and large existing faults can conspire to produce large earthquakes in volcanic areas.

6.6 A conceptual model for magma-tectonic interactions during the 2012-2019 eruption at Sabancaya

In our conceptual model for Sabancaya, a critically fluid saturated crust keeps preexisting tectonic faults close to failure. The stress perturbation from an incipient magmatic intrusion creates a fluid pressure pulse that rapidly destabilizes regional faults, leading to a dramatic uptick in seismicity. As the intrusion grows in size, static stress transfer from the inflation drives creep and pushes faults closer to failure, helped along by regionally high pore fluid pressures. Figure 11 depicts the stages of unrest at Sabancaya for the most recent episode of eruptive activity.

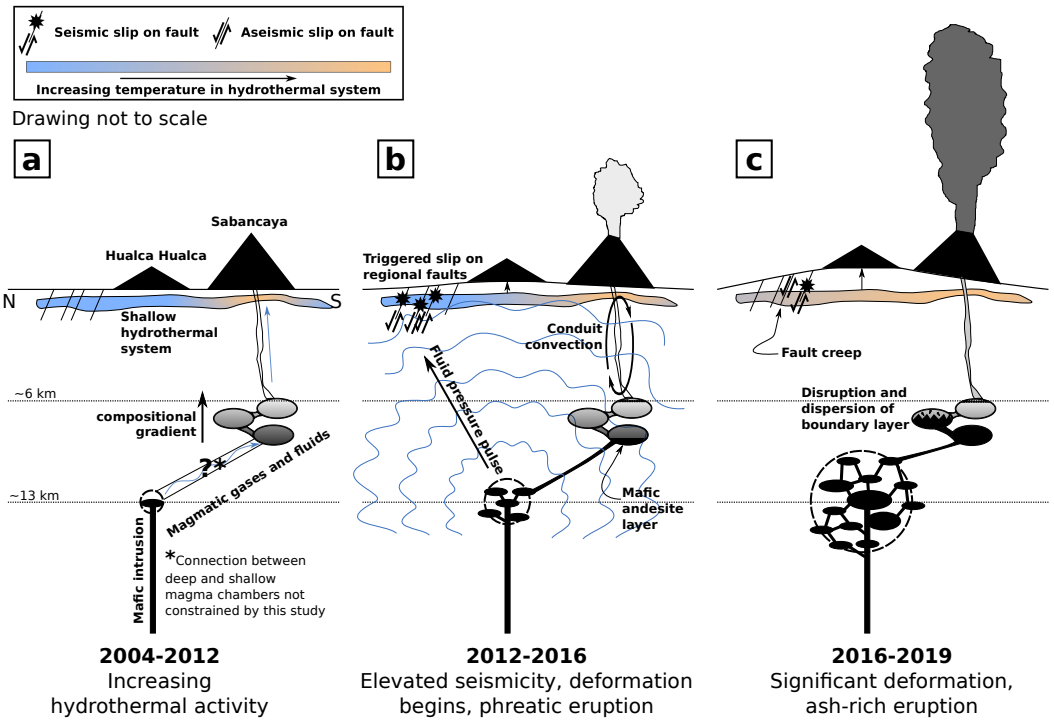

Figure 11. Conceptual model for 2012-2019 eruptive sequence at Sabancaya. See text for explanation.

.

First (Figure 11a), a mafic intrusion around 2011-2012 (thermal and degassing anomalies, Figure 10) at ~13 km depth (InSAR modeled deep inflation, Figure 4) brings a fresh charge of heat and magmatic gasses into the magmatic plumbing system beneath Hualca Hualca and Sabancaya, reactivating the shallow dacitic magma chamber at ~6 km depth [petrologic data, *Gerbe and Thouret*, 2004]. Heat and magmatic gasses from the dacitic magma chamber travel along pre-existing permeable pathways in the volcanic conduit at Sabancaya [*Moussallam et al.*, 2017], causing thermal anomalies and elevated degassing at Sabancaya (Figure 11a). This is consistent with the increase between 2011 and 2012 in thermal and SO_2 output at Sabancaya (Figure 10), the depth of the best-fit model for the InSAR time series (Figure 4), and the petrologic evidence for magma mixing between dacite and a mafic intrusion in the 1990-1998 eruption in *Gerbe and Thouret* [2004].

Second, pressure in the zone of mafic magma storage builds sufficiently to cause a stress perturbation that creates a fluid pressure pulse [e.g., *White and McCausland*, 2016], causing tectonic earthquakes on several regional faults (Figure 11b). These earthquakes preferentially occur to the north of Sabancaya [Figure 1, and Figure 1 of *Jay et al.*, 2015], closer to the source of the stress perturbation (the deep inflation source, Figure 4). Deformation from the mafic intrusion begins to be detectable via InSAR (Figure 10a). We note that the intrusion rate prior to 2013 was likely low enough to be undetectable with the limited InSAR data available during this time period (Figure 10a). A layer of mafic andesite forms at the base of the shallow storage zone [mafic enclaves in tephra from 1990-1998 eruption, *Gerbe and Thouret*, 2004]. The heat and magmatic gasses from the undegassed mafic magma [e.g., *Edmonds et al.*, 2001, 2019] drive convection in the conduit of Sabancaya [*Moussallam et al.*, 2017], leading to a steady hydrothermal plume and phreatic eruption, consistent with sustained high temperatures between 2012 and 2016 (Figure 10).

Finally, disruption and dispersion of the mafic andesite layer in the magma reservoir lead to higher intensity ash rich eruptions [Figure 11c of this study, *Gerbe and Thouret*,

2004]. Static stress from the now larger intrusion drives long-lived creep, in agreement with this study's InSAR observations of long-term aseismic slip (Figure 8) and static stress calculations(Figure S9). The sustained elevated heat flow eventually reactivates hydrothermal activity at Hualca Hualca [new thermal anomaly at Hualca Hualca in 2017, Figure 10 of this study, *Macedo*, 2018], leading to higher pore pressures and slip on faults in the hydrothermally active areas [Figures 3 and 9 of this study, *Macedo*, 2018].

This conceptual model pulls together evidence from InSAR, gas and thermal monitoring, seismic records, and petrology to explain two puzzling features of volcanic activity at Sabancaya: the inflation source that is offset from the eruption in both time and space, and the strong tectonic seismicity observed during eruptive periods. A mafic intrusion at depth, centered beneath Hualca Hualca, with a more "closed" behavior [e.g., *Chaussard et al.*, 2013] that perturbs a shallow, more "open" magma reservoir explains why eruptions at Sabancaya are accompanied by offset inflation that does not directly correspond to changes in eruptive activity at the surface.

7 Conclusion

We present an updated time series of deformation at Sabancaya volcano that captures deformation from volcanic inflation, two earthquakes, and fault creep, with the following key results:

1. InSAR-derived surface deformation times series data reveal a broad area of uplift north of Sabancaya with ongoing deformation from approximately 2013 through 2019. The best fit model for the uplift is a spherical inflation source centered 7 km NNW of Sabancaya with a depth of 13-14 km and a volume change rate of 0.04 to 0.05 km^3 yr^{-1}.
2. The best fit source models for surface deformation from two earthquakes north of Sabancaya in January and April of 2017 are NW striking normal faults dipping to the NE, similar to mapped tectonic faults in the area.
3. Our surface deformation times series reveal aseismic creep on three faults NW of Sabancaya. Of these faults, the Mojopampa fault exhibits long-lived post-seismic creep lasting for at least six years.
4. We find deformation from triggered slip on regional tectonic faults in response to large earthquakes in 1998 and 2013 in interferograms spanning these events.
5. Coulomb static stress changes from the modeled inflation source at Sabancaya are positive for the long-lived creeping fault and the two 2017 earthquakes.

We conclude that the deep seated inflation beneath Hualca Hualca is evidence of a laterally and vertically complex magma plumbing system beneath Sabancaya and Hualca Hualca. We argue that the deep seated inflation observed at Hualca Hualca represents mafic recharge of the system at depth, as in the model proposed by *Gerbe and Thouret* [2004]. We further speculate that these mafic intrusions at depth destabilize the magmatic plumbing system, pushing it towards eruption.

This study represents a semi-quantitative test of the "distal VTs" framework for understanding precursory seismic activity as put forward by *White and McCausland* [2016]. We argue that the key conditions for generating large magnitude seismicity in volcanic areas are significant magmatic inflation, extensive hydrothermal activity, and offset uplift beneath an area of low heat flow that favors the formation of larger faults.

InSAR observations spanning nearly three decades, and ground and satellite observations of hydrothermal activity, are key for our conceptual model of the 2013-2019 eruption at Sabancaya. InSAR-observed triggered slip in response to large earthquakes, and satellite and ground observations of extensive hydrothermal activity around Sabancaya, support our argument for a highly fractured, fluid saturated crust perpetually at a critical state of stress

in the region around Sabancaya. In our model, the stress perturbation from a magma intrusion at 13-14 km depth, first inferred via satellite thermal and degassing anomalies in 2011-2012 and later detectable via InSAR in 2013, triggers seismicity on regional tectonic faults in 2013 via a fluid pressure pulse. As the intrusion continues from 2013 through 2019, high regional fluid pore pressures, evident through satellite and ground observations in 2017 of the reinvigorated hydrothermal system at Hualca Hualca, also facilitate creep driven by static stress transfer from the deep inflation source. Static stress transfer from the ongoing intrusion is also sufficient to promote additional seismogenic slip on faults north of Hualca Hualca.

Acknowledgments

P.G.M., K.R., and M.E.P. were partly supported by grant NNX16AK87G issued through NASA's Science Mission Directorate's Earth Science Division. F.D. was supported by the NASA ESSF program for PhD fellowships and by a Centre National D'Études Spatiales (CNES) postdoctoral grant. M.B. was supported by an appointment to the NASA Postdoctoral Program at the Jet Propulsion Laboratory, administered by the Universities Space and Research Association (USRA) through a contract with NASA. We thank the Italian Space Agency (ASI) for providing COSMO-SkyMed data for this project. Original COSMO-SkyMed product ASI Agenzia Spaziale Italiana (2014–2019). CSK data were provided by an agreement between Agenzia Spaziale Italiana (ASI) and JPL. We acknowledge the CEOS volcano pilot project and the German Space Agency for TSX/TDX data from that project. The European Space Agency provided Sentinel-1, ERS-1/2 and Envisat data. By the acceptance of this paper, data will available via the Zenodo repository (https://zenodo.org/).

References

Abers, G. A. (2009), Slip on shallow-dipping normal faults, *Geology*, *37*(8), 767–768, doi: 10.1130/focus082009.1.

Acocella, V. (2007), Understanding caldera structure and development: An overview of analogue models compared to natural calderas, *Earth-Science Reviews*, *85*(3), 125–160, doi:10.1016/j.earscirev.2007.08.004.

Agram, P., R. Jolivet, M. Simons, and B. Riel (2012), GIAnT-generic InSAR analysis toolbox, in *AGU Fall Meeting Abstracts*, vol. 43, p. 0897.

Anccasi Figueroa, R. M., M. A. Ortega Gonzáles, B. Ccallata Pacsi, and R. Machacca Puma (2018), Actividad sísmica distal en el volcán Sabancaya (2015 - 2017), *Repositorio Institucional INGEMMET*.

Antayhua, Y., H. Tavera, and I. Bernal Esquia (2001), Análisis de la actividad sísmica en la región del volcán Sabancaya (Arequipa), *Repositorio institucional - IGP*.

Antayhua, Y., H. Tavera, I. Bernal Esquia, H. Palza, and V. Aguilar (2002), Localización hipocentrales y características de la fuente de los sismos de Maca (1991), Sepina (1992) y Cabanaconde (1998) Región Volcánica Sabancaya (Arequipa), *Repositorio institucional - IGP*.

Avouac, J.-P. (2015), From Geodetic Imaging of Seismic and Aseismic Fault Slip to Dynamic Modeling of the Seismic Cycle, *Annual Review of Earth and Planetary Sciences*, *43*(1), 233–271, doi:10.1146/annurev-earth-060614-105302.

Barnhart, W. D., and R. B. Lohman (2010), Automated fault model discretization for inversions for coseismic slip distributions, *Journal of Geophysical Research: Solid Earth*, *115*(B10), doi:10.1029/2010JB007545.

Benavente, C., F. Delgado, E. Aguirre, L. Albinez, and L. Audin (2016), Mapa Neotectónico Región Arequipa.

Benavente Escobar, C. L., G. F. Delgado Madera, B. García Fernández Baca, E. M. Aguirre Alegre, and L. Audin (2018), Neotectónica, evolución del relieve y peligro sísmico en la región Arequipa - [Boletín C 64], *Repositorio Institucional INGEMMET*.

Berardino, P., G. Fornaro, R. Lanari, and E. Sansosti (2002), A new algorithm for surface deformation monitoring based on small baseline differential SAR interferograms, *IEEE Transactions on Geoscience and Remote Sensing*, *40*(11), 2375–2383, doi:10.1109/TGRS.2002.803792.

Byrdina, S., D. Ramos, J. Vandemeulebrouck, P. Masias, A. Revil, A. Finizola, K. Gonzales Zuñiga, V. Cruz, Y. Antayhua, and O. Macedo (2013), Influence of the regional topography on the remote emplacement of hydrothermal systems with examples of Ticsani and Ubinas volcanoes, Southern Peru, *Earth and Planetary Science Letters*, *365*, 152–164, doi:10.1016/j.epsl.2013.01.018.

Bürgmann, R. (2018), The geophysics, geology and mechanics of slow fault slip, *Earth and Planetary Science Letters*, *495*, 112–134, doi:10.1016/j.epsl.2018.04.062.

Carn, S. A., V. E. Fioletov, C. A. McLinden, C. Li, and N. A. Krotkov (2017), A decade of global volcanic SO 2 emissions measured from space, *Scientific Reports*, *7*(1), 1–12, doi:10.1038/srep44095.

Cashman, K., and J. Biggs (2014), Common processes at unique volcanoes—a volcanological conundrum, *Frontiers in Earth Science*, *2*, doi:10.3389/feart.2014.00028.

Cashman, K. V., R. S. J. Sparks, and J. D. Blundy (2017), Vertically extensive and unstable magmatic systems: A unified view of igneous processes, *Science*, *355*(6331), eaag3055, doi:10.1126/science.aag3055.

Chadwick, W. W., D. J. Geist, S. Jónsson, M. Poland, D. J. Johnson, and C. M. Meertens (2006), A volcano bursting at the seams: Inflation, faulting, and eruption at Sierra Negra volcano, Galápagos, *Geology*, *34*(12), 1025–1028, doi:10.1130/G22826A.1.

Chaussard, E., F. Amelung, and Y. Aoki (2013), Characterization of open and closed volcanic systems in Indonesia and Mexico using InSAR time series, *Journal of Geophysical Research: Solid Earth*, *118*(8), 3957–3969, doi:10.1002/jgrb.50288.

Chen, C. W., and H. A. Zebker (2001), Two-dimensional phase unwrapping with use of statistical models for cost functions in nonlinear optimization, *JOSA A*, *18*(2), 338–351, doi:10.1364/JOSAA.18.000338.

Comeau, M. J., M. J. Unsworth, and D. Cordell (2016), New constraints on the magma distribution and composition beneath Volcán Uturuncu and the southern Bolivian Altiplano from magnetotelluric data, *Geosphere*, *12*(5), 1391–1421, doi:10.1130/GES01277.1.

Cruz, L., E. L. Taipe Maquerhua, and R. Miranda Cruz (2018), Asociación de la deformación registrada con GNSS CORS con las intrusiones magmáticas en el volcán Sabancaya durante el 2017, *Repositorio Institucional INGEMMET*.

Dalmayrac, B., and P. Molnar (1981), Parallel thrust and normal faulting in Peru and constraints on the state of stress, *Earth and Planetary Science Letters*, *55*(3), 473–481, doi:10.1016/0012-821X(81)90174-6.

Delgado, F., M. E. Pritchard, S. Ebmeier, P. González, and L. Lara (2017), Recent unrest (2002–2015) imaged by space geodesy at the highest risk Chilean volcanoes: Villarrica, Llaima, and Calbuco (Southern Andes), *Journal of Volcanology and Geothermal Research*, *344*(Supplement C), 270–288, doi:10.1016/j.jvolgeores.2017.05.020.

Delgado, F., M. Pritchard, S. Samsonov, and L. Córdova (2018), Renewed Posteruptive Uplift Following the 2011–2012 Rhyolitic Eruption of Cordón Caulle (Southern Andes, Chile): Evidence for Transient Episodes of Magma Reservoir Recharge During 2012–2018, *Journal of Geophysical Research: Solid Earth*, *123*(11), 9407–9429, doi:10.1029/2018JB016240.

Devlin, S., B. L. Isacks, M. E. Pritchard, W. D. Barnhart, and R. B. Lohman (2012), Depths and focal mechanisms of crustal earthquakes in the central Andes determined from teleseismic waveform analysis and InSAR, *Tectonics*, *31*(2), doi:10.1029/2011TC002914.

Ebmeier, S. K., B. J. Andrews, M. C. Araya, D. W. D. Arnold, J. Biggs, C. Cooper, E. Cottrell, M. Furtney, J. Hickey, J. Jay, R. Lloyd, A. L. Parker, M. E. Pritchard, E. Robertson, E. Venzke, and J. L. Williamson (2018), Synthesis of global satellite ob-

servations of magmatic and volcanic deformation: implications for volcano monitoring & the lateral extent of magmatic domains, *Journal of Applied Volcanology*, *7*(1), 2, doi:10.1186/s13617-018-0071-3.

Edmonds, M., D. Pyle, and C. Oppenheimer (2001), A model for degassing at the Soufrière Hills Volcano, Montserrat, West Indies, based on geochemical data, *Earth and Planetary Science Letters*, *186*(2), 159–173, doi:10.1016/S0012-821X(01)00242-4.

Edmonds, M., A. Aiuppa, M. Humphreys, R. Moretti, G. Giudice, R. S. Martin, R. A. Herd, and T. Christopher (2010), Excess volatiles supplied by mingling of mafic magma at an andesite arc volcano, *Geochemistry, Geophysics, Geosystems*, *11*(4), doi:10.1029/2009GC002781.

Edmonds, M., K. V. Cashman, M. Holness, and M. Jackson (2019), Architecture and dynamics of magma reservoirs, *Philosophical Transactions of the Royal Society A: Mathematical, Physical and Engineering Sciences*, *377*(2139), 20180,298, doi:10.1098/rsta.2018.0298.

Farr, T. G., P. A. Rosen, E. Caro, R. Crippen, R. Duren, S. Hensley, M. Kobrick, M. Paller, E. Rodriguez, L. Roth, D. Seal, S. Shaffer, J. Shimada, J. Umland, M. Werner, M. Oskin, D. Burbank, and D. Alsdorf (2007), The Shuttle Radar Topography Mission, *Reviews of Geophysics*, *45*(2), doi:10.1029/2005RG000183.

Finnegan, N. J., M. E. Pritchard, R. B. Lohman, and P. R. Lundgren (2008), Constraints on surface deformation in the Seattle, WA, urban corridor from satellite radar interferometry time-series analysis, *Geophysical Journal International*, *174*(1), 29–41, doi:10.1111/j.1365-246X.2008.03822.x.

Frietsch, M., A. M. G. Ferreira, G. J. Funning, and J. Weston (2019), Multiple fault modelling combining seismic and geodetic data: the importance of simultaneous subevent inversions, *Geophysical Journal International*, *218*(2), 958–976, doi:10.1093/gji/ggz205.

Gaherty, J. B., W. Zheng, D. J. Shillington, M. E. Pritchard, S. T. Henderson, P. R. N. Chindandali, H. Mdala, A. Shuler, N. Lindsey, S. J. Oliva, S. Nooner, C. A. Scholz, D. Schaff, G. Ekström, and M. Nettles (2019), Faulting processes during early-stage rifting: seismic and geodetic analysis of the 2009–2010 Northern Malawi earthquake sequence, *Geophysical Journal International*, *217*(3), 1767–1782, doi:10.1093/gji/ggz119.

Gerbe, M.-C., and J.-C. Thouret (2004), Role of magma mixing in the petrogenesis of tephra erupted during the 1990–98 explosive activity of Nevado Sabancaya, southern Peru, *Bulletin of Volcanology*, *66*(6), 541–561, doi:10.1007/s00445-004-0340-3.

Global Volcanism Program (1988), Report on Sabancaya (Peru), *Tech. Rep. 13:6*, Smithsonian Institution.

Global Volcanism Program (2000), Report on Sabancaya (Peru), *Tech. Rep. 25:5*, Smithsonian Institution.

Global Volcanism Program (2013), Volcanoes of the World, v. 4.8.0., smithsonian Institution.

Global Volcanism Program (2016), Report on Sabancaya (Peru), *Tech. Rep. 41:5*, Smithsonian Institution.

Global Volcanism Program (2017), Report on Sabancaya (Peru), *Tech. Rep. 42:5*, Smithsonian Institution.

Goldstein, R. M., H. A. Zebker, and C. L. Werner (1988), Satellite radar interferometry: Two-dimensional phase unwrapping, *Radio Science*, *23*(4), 713–720, doi:10.1029/RS023i004p00713.

Hayes, G. P., D. J. Wald, and R. L. Johnson (2012), Slab1.0: A three-dimensional model of global subduction zone geometries, *Journal of Geophysical Research: Solid Earth*, *117*(B1), doi:10.1029/2011JB008524.

Henderson, S. T., and M. E. Pritchard (2013), Decadal volcanic deformation in the Central Andes Volcanic Zone revealed by InSAR time series, *Geochemistry, Geophysics, Geosystems*, *14*(5), 1358–1374, doi:10.1002/ggge.20074.

Henderson, S. T., and M. E. Pritchard (2017), Time-dependent deformation of Uturuncu volcano, Bolivia, constrained by GPS and InSAR measurements and implications for

source models, *Geosphere*, *13*(6), 1–21, doi:10.1130/GES01203.1.

Holtkamp, S. G., M. E. Pritchard, and R. B. Lohman (2011), Earthquake swarms in South America, *Geophysical Journal International*, *187*(1), 128–146, doi:10.1111/j.1365-246X.2011.05137.x.

Huaman-Rodrigo, D., J. Chorowicz, B. Deffontaines, R. Guillande, and J. Rudant (1993), Cadre structural et risques géologiques étudiés à l'aide de l'imagerie spatiale: la région du Colca (Andes du sud Pérou), *BULLETIN-SOCIETE GEOLOGIQUE DE FRANCE*, *164*, 807–807.

Instituto Geofísico del Perú (2017), Investigación y monitoreo de volcanes activos en el sur del Perú. Reporte técnico especial 2016, *Tech. rep.*, Instituto Geofísico del Perú Observatorio Vulcanológico del Sur.

Jay, J. A. (2014), A Geophysical Survey of Active Volcanism in the Central and Southern Andes, Ph.D., Cornell University.

Jay, J. A., F. J. Delgado, J. L. Torres, M. E. Pritchard, O. Macedo, and V. Aguilar (2015), Deformation and seismicity near Sabancaya volcano, southern Peru, from 2002 to 2015, *Geophysical Research Letters*, *42*(8), 2780–2788, doi:10.1002/2015GL063589.

Kagan, Y. Y., and D. D. Jackson (1991), Long-term earthquake clustering, *Geophysical Journal International*, *104*(1), 117–133, doi:10.1111/j.1365-246X.1991.tb02498.x.

Kern, C., P. Masias, F. Apaza, K. A. Reath, and U. Platt (2017), Remote measurement of high preeruptive water vapor emissions at Sabancaya volcano by passive differential optical absorption spectroscopy, *Journal of Geophysical Research: Solid Earth*, *122*(5), 3540–3564, doi:10.1002/2017JB014020.

King, G. C. P., R. S. Stein, and J. Lin (1994), Static stress changes and the triggering of earthquakes, *Bulletin of the Seismological Society of America*, *84*(3), 935–953.

Lienkaemper, J. J., and F. S. McFarland (2017), Long-Term Afterslip of the 2004 M 6.0 Parkfield, California, Earthquake—Implications for Forecasting Amount and Duration of Afterslip on Other Major Creeping FaultsLong-Term Afterslip of the 2004 M 6.0 Parkfield Earthquake, *Bulletin of the Seismological Society of America*, *107*(3), 1082–1093, doi:10.1785/0120160321.

Lin, Y.-n. N., M. Simons, E. A. Hetland, P. Muse, and C. DiCaprio (2010), A multiscale approach to estimating topographically correlated propagation delays in radar interferograms, *Geochemistry, Geophysics, Geosystems*, *11*(9), doi:10.1029/2010GC003228.

Lohman, R. B., and M. Simons (2005), Some thoughts on the use of InSAR data to constrain models of surface deformation: Noise structure and data downsampling, *Geochemistry, Geophysics, Geosystems*, *6*(1), doi:10.1029/2004GC000841.

Lundgren, P., M. Nikkhoo, S. V. Samsonov, P. Milillo, F. Gil-Cruz, and J. Lazo (2017), Source model for the Copahue volcano magma plumbing system constrained by InSAR surface deformation observations, *Journal of Geophysical Research: Solid Earth*, *122*(7), 5729–5747, doi:10.1002/2017JB014368.

Macedo, O. (2018), Observaciones de campo en la zona de Pinchollo al norte del volcán Sabancaya, *Informe Técnico*, Instituto Geofísico del Perú.

Machacca Puma, R., M. A. Ortega Gonzáles, R. Miranda Cruz, F. E. Apaza Choquehuayta, I. A. Lazarte Zerpa, P. J. Masías Alvarez, D. A. Ramos Palomino, B. Ccallata Pacsi, R. M. Anccasi Figueroa, E. L. Taipe Maquerhua, and L. Cruz (2018), Monitoreo Multi-paramétrico del volcán Sabancaya y evolución del proceso eruptivo 2016-2017, in *Libro de resúmenes: VIII Foro Internacional los Volcanes y su Impacto, Arequipa, 26 y 27 de abril del 2018*, pp. 105–108, Instituto Geológico, Minero y Metalúrgico – INGEMMET, Arequipa, Peru.

Machare, J., C. H. Fenton, M. N. Machette, A. Lavenu, C. Costa, and R. L. Dart (2003), Database and Map of Quaternary Faults and Folds in Peru and its Offshore Region, *USGS Numbered Series 2003-451*, United States Geological Survey.

Manrique Llerena, N., I. A. Lazarte Zerpa, C. Sandoval, K. Arnold, M. A. Rivera Porras, and R. Aguilar Contreras (2018), Actividad del volcán Sabancaya (Perú) 2016-2017: Características de las emisiones de ceniza y análisis granulométrico, *Libro de*

resúmenes: VIII Foro Internacional los Volcanes y su Impacto, Arequipa, 26 y 27 de abril del 2018.

Marco, S., M. Stein, A. Agnon, and H. Ron (1996), Long-term earthquake clustering: A 50,000-year paleoseismic record in the Dead Sea Graben, *Journal of Geophysical Research: Solid Earth*, *101*(B3), 6179–6191, doi:10.1029/95JB01587.

Mellors, R. J., H. Magistrale, P. Earle, and A. Cogbill (2004), Comparison of Four Moderate-Size Earthquakes in Southern California Using Seismology and InSAR, *Bulletin of the Seismological Society of America*, *94*(6), 2004–2014, doi:10.1785/0120020219.

Mering, C., D. Huaman-Rodrigo, J. Chorowicz, B. Deffontaines, and R. Guillande (1996), New data on the geodynamics of southern Peru from computerized analysis of SPOT and SAR ERS-1 images, *Tectonophysics*, *259*(1), 153–169, doi:10.1016/0040-1951(96)00034-0.

Miller, S. A., C. Collettini, L. Chiaraluce, M. Cocco, M. Barchi, and B. J. P. Kaus (2004), Aftershocks driven by a high-pressure CO 2 source at depth, *Nature*, *427*(6976), 724–727, doi:10.1038/nature02251.

Mogi, K. (1958), Relations between the eruptions of various volcanoes and the deformations of the ground surfaces around them, *B. Earthq. Res. I.*, *36*, 99–134.

Morales Rivera, A. M., F. Amelung, and P. Mothes (2016), Volcano deformation survey over the Northern and Central Andes with ALOS InSAR time series, *Geochemistry, Geophysics, Geosystems*, *17*(7), 2869–2883, doi:10.1002/2016GC006393.

Moussallam, Y., G. Tamburello, N. Peters, F. Apaza, C. I. Schipper, A. Curtis, A. Aiuppa, P. Masias, M. Boichu, S. Bauduin, T. Barnie, P. Bani, G. Giudice, and M. Moussallam (2017), Volcanic gas emissions and degassing dynamics at Ubinas and Sabancaya volcanoes; implications for the volatile budget of the central volcanic zone, *Journal of Volcanology and Geothermal Research*, *343*, 181–191, doi:10.1016/j.jvolgeores.2017.06.027.

Newman, A. V., T. H. Dixon, and N. Gourmelen (2006), A four-dimensional viscoelastic deformation model for Long Valley Caldera, California, between 1995 and 2000, *Journal of Volcanology and Geothermal Research*, *150*(1), 244–269, doi:10.1016/j.jvolgeores.2005.07.017.

Nishimura, T., S. Fujiwara, M. Murakami, M. Tobita, H. Nakagawa, T. Sagiya, and T. Tada (2001), The M6.1 earthquake triggered by volcanic inflation of Iwate Volcano, northern Japan, observed by satellite radar interferometry, *Geophysical Research Letters*, *28*(4), 635–638, doi:10.1029/2000GL012022.

Okada, Y. (1985), Surface deformation due to shear and tensile faults in a half-space, *Bulletin of the Seismological Society of America*, *75*(4), 1135–1154.

Perfettini, H., and J.-P. Avouac (2004), Postseismic relaxation driven by brittle creep: A possible mechanism to reconcile geodetic measurements and the decay rate of aftershocks, application to the Chi-Chi earthquake, Taiwan, *Journal of Geophysical Research: Solid Earth*, *109*(B2), doi:10.1029/2003JB002488.

Poland, M. P., A. Peltier, A. Bonforte, and G. Puglisi (2017), The spectrum of persistent volcanic flank instability: A review and proposed framework based on Kīlauea, Piton de la Fournaise, and Etna, *Journal of Volcanology and Geothermal Research*, *339*, 63–80, doi:10.1016/j.jvolgeores.2017.05.004.

Pritchard, M. E., and M. Simons (2004), An InSAR-based survey of volcanic deformation in the central Andes, *Geochemistry, Geophysics, Geosystems*, *5*(2), Q02,002, doi:10.1029/2003GC000610.

Pritchard, M. E., J. Biggs, C. Wauthier, E. Sansosti, D. W. D. Arnold, F. Delgado, S. K. Ebmeier, S. T. Henderson, K. Stephens, C. Cooper, K. Wnuk, F. Amelung, V. Aguilar, P. Mothes, O. Macedo, L. E. Lara, M. P. Poland, and S. Zoffoli (2018), Towards coordinated regional multi-satellite InSAR volcano observations: results from the Latin America pilot project, *Journal of Applied Volcanology*, *7*(1), 5, doi:10.1186/s13617-018-0074-0.

Puma, N., J. Torres, O. Macedo, R. Centeno, J. Del Carpio, and J. Cruz (2016), Evolución de la actividad sismo-volcánica en la zona del volcán Sabancaya (2013-2016), in *XVIII Congreso Peruano de Geología. Sociedad Geologica del Perú*.

Rankin, A. J. (2012), Predicted ash hazards from potential eruptions at Nevado Sabancaya, Peru: HYSPLIT and remote sensing, Master's thesis, State University of New York at Buffalo, United States – New York.

Reath, K., M. Pritchard, M. Poland, F. Delgado, S. Carn, D. Coppola, B. Andrews, S. K. Ebmeier, E. Rumpf, S. Henderson, S. Baker, P. Lundgren, R. Wright, J. Biggs, T. Lopez, C. Wauthier, S. Moruzzi, A. Alcott, R. Wessels, J. Griswold, S. Ogburn, S. Loughlin, F. Meyer, G. Vaughan, and M. Bagnardi (2019a), Thermal, Deformation, and Degassing Remote Sensing Time Series (CE 2000–2017) at the 47 most Active Volcanoes in Latin America: Implications for Volcanic Systems, *Journal of Geophysical Research: Solid Earth*, *0*(0), doi:10.1029/2018JB016199.

Reath, K., M. E. Pritchard, S. Moruzzi, A. Alcott, D. Coppola, and D. Pieri (2019b), The AVTOD (ASTER Volcanic Thermal Output Database) Latin America archive, *Journal of Volcanology and Geothermal Research*, *376*, 62–74, doi:10.1016/j.jvolgeores.2019.03.019.

Riddick, S. N., and D. A. Schmidt (2011), Time-dependent changes in volcanic inflation rate near Three Sisters, Oregon, revealed by InSAR, *Geochemistry, Geophysics, Geosystems*, *12*(12), doi:10.1029/2011GC003826.

Rodríguez, A., and M. Uribe (1994), Participación del Instituto Geofísico del Perú en relación con la reactivación del volcán Sabancaya, Provincia de Caylloma, Región Arequipa, *Informe División de Sismología y Gravimetría, IGP-Arequipa*.

Rosen, P. A., S. Hensley, G. Peltzer, and M. Simons (2004), Updated repeat orbit interferometry package released, *Eos, Transactions American Geophysical Union*, *85*(5), 47–47, doi:10.1029/2004EO050004.

Rosen, P. A., E. M. Gurrola, P. S. Agram, G. F. Sacco, and M. Lavalle (2015), The InSAR Scientific Computing Environment (ISCE): A Python Framework for Earth Science, in *AGU Fall Meeting Abstracts*, vol. 11, pp. IN11C–1789.

Samaniego, P., M. Rivera, J. Mariño, H. Guillou, C. Liorzou, S. Zerathe, R. Delgado, P. Valderrama, and V. Scao (2016), The eruptive chronology of the Ampato–Sabancaya volcanic complex (Southern Peru), *Journal of Volcanology and Geothermal Research*, *323*, 110–128, doi:10.1016/j.jvolgeores.2016.04.038.

Sambridge, M. (1999), Geophysical inversion with a neighbourhood algorithm—I. Searching a parameter space, *Geophysical Journal International*, *138*(2), 479–494, doi:10.1046/j.1365-246X.1999.00876.x.

Schmidt, D. A., and R. Bürgmann (2008), Predicted reversal and recovery of surface creep on the Hayward fault following the 1906 San Francisco earthquake, *Geophysical Research Letters*, *35*(19), doi:10.1029/2008GL035270.

Segall, P., and J. R. Rice (1995), Dilatancy, compaction, and slip instability of a fluid-infiltrated fault, *Journal of Geophysical Research: Solid Earth*, *100*(B11), 22,155–22,171, doi:10.1029/95JB02403.

Singer, B. S., H. L. Mével, J. M. Licciardi, L. Córdova, B. Tikoff, N. Garibaldi, N. L. Andersen, A. K. Diefenbach, and K. L. Feigl (2018), Geomorphic expression of rapid Holocene silicic magma reservoir growth beneath Laguna del Maule, Chile, *Science Advances*, *4*(6), eaat1513, doi:10.1126/sciadv.aat1513.

Sébrier, M., J. L. Mercier, F. Mégard, G. Laubacher, and E. Carey-Gailhardis (1985), Quaternary normal and reverse faulting and the state of stress in the central Andes of south Peru, *Tectonics*, *4*(7), 739–780, doi:10.1029/TC004i007p00739.

Taipe Maquerhua, E. L., R. Miranda Cruz, and J. Díaz Apaza (2016), Análisis de deformación del volcán Sabancaya con datos GPS, periodo 2015, *Instituto Geológico, Minero y Metalúrgico – INGEMMET*.

Toda, S., and R. Stein (2003), Toggling of seismicity by the 1997 Kagoshima earthquake couplet: A demonstration of time-dependent stress transfer, *Journal of Geophysical Re-*

search: Solid Earth, *108*(B12), doi:10.1029/2003JB002527.

Wang, K., X. Xu, and Y. Fialko (2017), Improving Burst Alignment in TOPS Interferometry With Bivariate Enhanced Spectral Diversity, *IEEE Geoscience and Remote Sensing Letters*, *14*(12), 2423–2427, doi:10.1109/LGRS.2017.2767575.

Wauthier, C., D. C. Roman, and M. P. Poland (2016), Joint analysis of geodetic and earthquake fault-plane solution data to constrain magmatic sources: A case study from Kīlauea Volcano, *Earth and Planetary Science Letters*, *455*, 38–48, doi:10.1016/j.epsl.2016.09.011.

Weston, J., A. M. G. Ferreira, and G. J. Funning (2011), Global compilation of interferometric synthetic aperture radar earthquake source models: 1. Comparisons with seismic catalogs, *Journal of Geophysical Research: Solid Earth*, *116*(B8), doi:10.1029/2010JB008131.

White, R., and W. McCausland (2016), Volcano-tectonic earthquakes: A new tool for estimating intrusive volumes and forecasting eruptions, *Journal of Volcanology and Geothermal Research*, *309*, 139–155, doi:10.1016/j.jvolgeores.2015.10.020.

Wimpenny, S., A. Copley, C. Benavente, and E. Aguirre (2018), Extension and Dynamics of the Andes Inferred From the 2016 Parina (Huarichancara) Earthquake, *Journal of Geophysical Research: Solid Earth*, *123*(9), 8198–8228, doi:10.1029/2018JB015588.

Xu, G., C. Xu, Y. Wen, and Z. Yin (2019), Coseismic and Postseismic Deformation of the 2016 MW 6.2 Lampa Earthquake, Southern Peru, Constrained by Interferometric Synthetic Aperture Radar, *Journal of Geophysical Research: Solid Earth*, *124*(4), 4250–4272, doi:10.1029/2018JB016572.

Yang, X.-M., P. M. Davis, and J. H. Dieterich (1988), Deformation from inflation of a dipping finite prolate spheroid in an elastic half-space as a model for volcanic stressing, *Journal of Geophysical Research: Solid Earth*, *93*(B5), 4249–4257, doi:10.1029/JB093iB05p04249.

Zobin, V. M. (2001), Seismic hazard of volcanic activity, *Journal of Volcanology and Geothermal Research*, *112*(1), 1–14, doi:10.1016/S0377-0273(01)00230-X.